Anticlockwise metamorphic paths at ca. 890–790 Ma from the NE Baidrag block, Mongolia, indicate back-arc compression at the Rodinia periphery

Pavla Štípská, Vít Peřestý, Igor Soejono, Karel Schulmann, R.C. Andrew Kylander-Clark, Carmen Aguilar, Stephen Collett, Martin Racek, Jitka Míková, Otgonbaatar Dorjsuren, et al.

Geoscience Frontiers 14 (2023) 101520

HOSTED BY

Contents lists available at ScienceDirect

Geoscience Frontiers

journal homepage: www.elsevier.com/locate/gsf

Research Paper

Anticlockwise metamorphic paths at ca. 890–790 Ma from the NE Baidrag block, Mongolia, indicate back-arc compression at the Rodinia periphery

Pavla Štípská [a,*], Vít Peřestý [b], Igor Soejono [a], Karel Schulmann [a,c], R.C. Andrew Kylander–Clark [d], Carmen Aguilar [e], Stephen Collett [a], Martin Racek [b], Jitka Míková [a], Otgonbaatar Dorjsuren [f], Nikol Novotná [a]

[a] Czech Geological Survey, 11821 Praha 1, Czech Republic
[b] Institute of Petrology and Structural Geology, Charles University in Prague, Albertov 6, Praha 2 12800, Czech Republic
[c] Institut Terre et Environnement de Strasbourg, UMR 7063 Université de Strasbourg—CNRS, 1 Rue Blessig, 67084 Strasbourg, Cedex, France
[d] Department of Earth Science, University of California, Santa Barbara, CA 93106, United States
[e] Department of Mineralogy, Petrology and Applied Geology, Faculty of Earth Science, University of Barcelona, 08028 Barcelona, Spain
[f] Institute of Geology, Mongolian Academy of Sciences, Labor Union Street, Songinokhairkhan District, Ulaanbaatar 18080, Mongolia

ARTICLE INFO

Article history:
Received 15 June 2022
Revised 14 October 2022
Accepted 26 November 2022
Available online 5 December 2022
Handling Editor: Stijn Glorie

Keywords:
Central Asian Orogenic Belt
Grenvillian-age metamorphism
Monazite in-situ U–Pb dating
Monazite REE composition
Zircon U–Pb dating
Thermodynamic modelling

ABSTRACT

The processes leading to the assembly of the Rodinia supercontinent through Grenvillian collisional orogeny are relatively well known. In contrast, accretionary orogenic processes occurring at the supercontinent periphery following Rodinia assembly are poorly understood. To fill this gap, we have identified metamorphic rocks in the Mongolia collage of the Central Asian Orogenic Belt, where numerous data testify for Meso- to Neoproterozoic magmatic reworking. The tectono-metamorphic evolution of the peri-Siberian tract of the Central Asian Orogenic Belt is mainly characterized by the late Proterozoic–early Cambrian (Baikalian) cycle. However, we document here a Tonian age metamorphism at the northern part of the Precambrian Baidrag block, previously considered as a typical example of the Baikalian metamorphic belt. This study incorporates zircon and in-situ monazite geochronology linked to *P-T* modelling of Grt-Sil-Ky migmatite gneiss and Grt-St micaschist. Grt-Sil-Ky gneiss records initial burial to the sillimanite stability field at ~720 °C and 6.0 kbar followed by further burial to the kyanite stability field at ~750 °C and ~9 kbar and decompression to ~650 °C and ~8 kbar. The Grt-St schist records initial burial to the staurolite stability field at ~620 °C and 6 kbar, followed by further burial to ~590 °C and 8.5 kbar. The monazite data yield a continuum of ^{207}Pb-corrected ^{238}U/^{206}Pb dates of ca. 926–768 Ma in the Grt-Sil-Ky gneiss, and ca. 937–754 Ma in the Grt-St schist. Based on monazite textural positon, internal zoning, and REE patterns, the time of prograde burial to 6.0 kbar under a thermal gradient of 27–32 °C/km is estimated at ca. 890–853 Ma. It is not clear whether such high-grade conditions prevailed until a phase of further burial under a geothermal gradient of 18–22 °C/km dated at ca. 835–815 Ma. The late monazite recrystallization at ca. 790 Ma is related to decompression. Additionally, monazite with dates of ca. 568–515 Ma occur as whole grains or as rims with sharp boundaries on Tonian monazite in Grt-St schist suggesting a minor Baikalian overprint. Metamorphic zircon rims with Th/U ratios of ~ 0.01–0.06 in Grt-Sil-Ky gneiss with 877 ± 7 Ma age, together with lower intercepts of detrital zircon discordia lines in both Grt-Sil-Ky gneiss and Grt-St schist further support the Tonian age of high-grade metamorphism. The anticlockwise *P-T* evolution is interpreted as a result of thickening of a supra-subduction extensional and hot edifice – probably of back-arc or arc type. This kind of prograde metamorphism has so far only been described on the northern part of the Tarim block and was interpreted to be a result of initiation of peri-Rodinian subduction of the Mirovoi Ocean. The geodynamic consequences of a unique discovery of Tonian metamorphism are discussed in terms of tectonic switch related to initiation of peri-Rodinian oceanic subduction during supercontinent assembly, followed by strong mechanical coupling potentially related to onset of Rodinia dispersal.

* Corresponding author.
E-mail address: pavla.stipska@geology.cz (P. Štípská).

https://doi.org/10.1016/j.gsf.2022.101520
1674-9871/

1. Introduction

The assembly of supercontinents arises through amalgamation of continental blocks relating to collisional orogeny, while at the supercontinent periphery, subduction of a peripheral or exterior ocean forms accretionary orogens (e.g. Murphy and Nance, 1991; Cawood and Buchan, 2007; Cawood et al., 2009). Accretionary orogens involve fore-arcs, magmatic arcs, back-arcs and accretionary wedges, which may deform during advancing and retreating subduction modes (Collins, 2002). In general, during a retreating mode, the upper plate is under a long-lasting extension and wide back-arc basins develop, while during an advancing mode, the upper plate is in compression and crustal thickening occurs (Collins, 2002; Lister and Forster, 2009). These processes involve important addition of juvenile magma in the arc system, melting of the back-arc crust and tectonic accretion of fertile material, which all can be affected by multiple phases of metamorphism and deformation (e.g. Jiang et al., 2019; Soejono et al., 2021). Cawood and Buchan (2007) proposed that the retreating subduction mode may continuously operate during amalgamation of a supercontinent, i.e. when a number of interior oceanic subduction systems exist between individual continental blocks. When these systems are closed, multiple plates became one plate and the subduction is relocated solely to the boundary between the supercontinent and its peripheral ocean. This may lead to the inception of advancing subduction mode (Cawood, 2005) and onset of formation of a peripheral accretionary system. When the supercontinent starts to disintegrate and a new interior ocean forms – the continental masses are pushed against their peripheral subduction zones, thereby producing mechanical coupling between the lower oceanic and upper continental plate leading to contractional orogeny (Cawood and Buchan, 2007).

In the case of the Rodinia supercontinent, it was proposed that its assembly resulted in the so-called Grenvillian orogeny between ca. 1300 Ma and 900 Ma when different crustal blocks amalgamated through "interior" collisional processes, while the break-up of the Rodinia "interior" through continental rifting and formation of paleo-Pacific ocean occurred at ca. 830–600 Ma (Li et al., 2008; Evans, 2009). Numerous studies devoted to the evolution of the interior parts of Rodinia have led to a relatively good understanding of its amalgamation and break-up (Li et al., 2008; Evans, 2013; and references therein).

In contrast, studies concerning the peripheral evolution are relatively few and are typically focused on geochemical and geochronological data from magmatic rocks or detrital zircon geochronology from sediments (e.g. Nance et al., 2014; Cawood et al., 2016; Skuzovatov et al., 2019), emplaced or deposited in an active margin setting (Cawood et al., 2010; Yao et al., 2019). These studies have identified significant magmatic activity during the early parts of the Neoproterozoic (1.0–0.8 Ga), and interpreted it as a result of the Mirovoi Ocean subduction beneath the Rodinia periphery (e.g. Li et al., 2008; Scotese, 2009). Nonetheless, metamorphic petrological studies of these early Neoproterozoic events are very rare (He et al., 2012; Wang et al., 2014; Ge et al., 2016; Haozheng et al., 2019; Ren et al., 2019, 2021; Soldner et al., 2020), and complicated owing to significant overprinting during late Neoproterozoic to late Paleozoic orogeny during the building of Pangea (e.g. Cutts et al., 2010; Ren et al., 2019, 2021). One of the principle areas where these Tonian tectono-metamorphic events have been documented is the late Neoproterozoic–late Paleozoic Central Asian Orogenic Belt (CAOB; Fig. 1) super-collage (Xiao et al., 2015, Xiao et al., 2018). The CAOB (Zonenshain, 1990) is located between the Siberia, Tarim and North China cratonic blocks (Fig. 1), which are typically assumed to have been

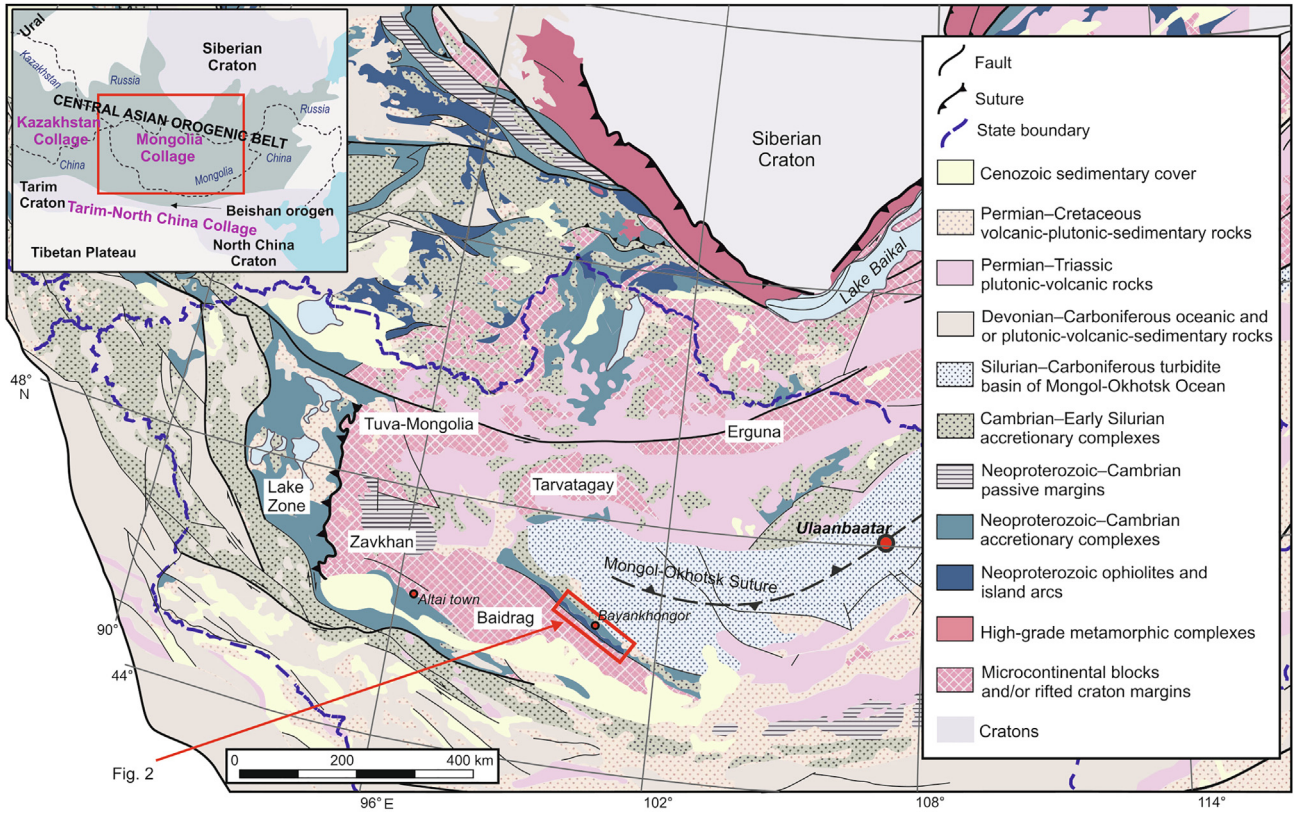

Fig. 1. Map of the Mongolian part of the CAOB (modified after Parfenov et al., 2003). The study region is indicated by rectangle, the inset shows the position of the CAOB with respect to main cratons.

located at the Rodinian periphery (e.g. Li et al., 2008), and can broadly be subdivided into three tectonic collages: the Tarim-North China, Kazakhstan and Mongolian collages (Xiao et al., 2015). This vast accretionary system consists of Precambrian basement blocks, late Proterozoic to Paleozoic arcs, back-arcs and accretionary complexes (Wilhem et al., 2012). These were progressively accreted to the Siberian nucleus (Windley et al., 2007) during two main Cambrian and Carboniferous tectonic cycles also referred as Caledonian and Hercynian. However, while the Paleozoic accretionary evolution of the CAOB super-collage is relatively well understood (e.g. Xiao et al., 2018), the pre-Paleozoic evolution is less known. This is compounded by proposed differences in the pre-Paleozoic paleogeography of the Tarim-North China and the Kazakhstan collages with respect to the Mongolian collage, which obscure our understanding of the evolution of the principal segments forming the CAOB super-collage (Xiao et al., 2015).

Recent investigations suggest that the northeastern Mongolia collage experienced Mesoproterozoic to Neoproterozoic magmatic reworking similar in age to magmatism affecting the southerly Tarim-North China and the westerly Kazakhstan collages (e.g. Huang et al., 2017). These data involve magmatic reworking in the Tuva, Zavkhan, Tarvatagay and Baidrag blocks (Fig. 1) (Kuzmichev et al., 2001; Demoux et al., 2009a; Kozakov et al., 2012, 2014; Bold et al., 2016; Buriánek et al., 2017; Skuzovatov, 2021). In addition, numerous Stenian to Tonian oceanic island arcs or other supra-subduction complexes dated between 1050 Ma and 760 Ma are located in between the Siberian craton and the CAOB super-collage (Rytsk et al., 2001; Khain et al., 2002; Gordienko et al., 2009; Shatsky et al., 2015). It is evident therefore, that the northern part of the Mongolian collage experienced a Stenian to Tonian supra-subduction event, which may be similar to that reported from the southerly Tarim-North China collage.

Nonetheless, no metamorphic rocks associated with these events have thus far been documented. Identifying such rocks and determining well-constrained *P-T-t* paths would aid in characterizing tectono-thermal processes at the Rodinia periphery and in establishing paleo-geographic links between the Mongolian collage and the Tarim-North China collage in Rodinia reconstructions. In search of a Stenian to Tonian tectono-metamorphic supra-subduction event we examined the northern margin of the central Baidrag block by means of combined petrological and monazite and zircon petro-chronological study of the metapelitic sequences. Here, metasedimentary rocks were supposedly affected by Barrovian metamorphism in the late Proterozoic (570–560 Ma, Kozakov et al., 2008), and reworked later by a high temperature (HT) early Cambrian event (Kozakov et al., 2012). However, our study shows that the earliest metamorphism records an anticlockwise *P-T* path and occurs in the early Neoproterozoic. These observations result in radical re-interpretation of the tectono-thermal and geodynamic evolution of the Baidrag block. The correlation with similar metamorphic evolutions affecting the Tarim block (He et al., 2012; Ge et al., 2016) or Tonian thermal event affecting the Beishan orogen in NW China (Soldner et al., 2020) are discussed in light of Grenvillian-age supra-subduction evolution of the northern margin of the Rodinia supercontinent.

2. Geological setting

The Baidrag block belongs to a string of Precambrian microcontinents exposed in the Mongolian collage: Tuva, Tarvatagay, Zavkhan in the NW and Erguna in the east, which are interpreted as fragments rifted from the Rodinia supercontinent (Fig. 1; e.g. Cocks and Torsvik, 2007; Wilhem et al., 2012). The NE–SW trending Baidrag block is composed of Archean to Mesoproterozoic variably deformed and metamorphosed rocks (Kozakov et al., 2007; Demoux et al., 2009b; Kröner et al., 2014) (Fig. 1). It is surrounded in both the NW and SE by Ediacaran to early Paleozoic units interpreted as relics of oceanic supra-subduction basins thrust over the basement during Paleozoic times (e.g. Buchan et al., 2001; Osozawa et al., 2008; Jian et al., 2010; Kröner et al., 2011; Yarmolyuk et al., 2011; Rudnev et al., 2012; Buriánek et al., 2017).

2.1. Geology of the NE margin of the Baidrag block

The NE margin of the Baidrag block is formed by four major NW–SE elongated lithotectonic zones (Fig. 2): Burd Gol zone, Bayankhongor zone, both intruded by Ediacaran–Cambrian plutons, Dzag zone of Silurian turbidites and Khangay zone of Devonian–Carboniferous turbidites (e.g. Demoux et al., 2009b).

The Baidrag basement is composed of metaigneous unit dominated by migmatitic tonalitic gneisses, amphibolite and pyroxene-bearing mafic gneisses and a mostly metasedimentary unit including amphibolite- to granulite-facies pyroxene-gneisses, leucocratic gneisses, olivine-bearing marbles, quartzites and garnet–biotite schists. The emplacement of the oldest igneous protoliths at 2890–2650 Ma was followed by ca. 2400–2310 Ma intrusions of pyroxene granodiorite, quartz diorite and biotite granite and 1850–1820 Ma emplacement of enstatite-bearing garnet granodiorite and granosyenite veins (Mitrofanov et al., 1985; Bibikova et al., 1990; Kozakov, 1993; Kotov et al., 1995; Demoux et al., 2009a) associated with ca. 1850 Ma granulite-facies metamorphism and magmatism (Demoux et al., 2009a).

The Burd Gol zone is a ~ 100 km long belt of volcanic-sedimentary rocks, interpreted as an accretionary complex, and intruded by Ediacaran–Cambrian granite. Its unmetamorphosed part crops out close to the Bumbuger village where the metaigneous gneisses are unconformably overlain by ~250 m thick sequence of quartzite and conglomerate followed by early Mesoproterozoic stromatolite-bearing limestone (Dergunov et al., 1997; Tomurtogoo and Gerel, 1999). In the Ulziit Gol transect (Fig. 2), the rock sequence is interpreted as a tectonic mélange (Buchan et al., 2001) consisting of basal quartzites, limestones and foliated black schists with up to hundred meters large lenses of limestone, sandstone, chert, bedded calci-turbidite, basalt, gabbro, andesite and subordinate rhyolite. Along the Taats Gol transect, granite gneiss with lenses of garnet-bearing metagabbro and amphibolite occur in the south, and biotite-rich gneiss, calc-silicate schist, quartzite, and garnet-bearing amphibolite in the north (Demoux et al., 2009a). Some of these crystalline rocks were tentatively considered to be derived from the Baidrag basement (Kozakov et al., 2007, 2012). The age of the sediments was previously determined as Mesoproterozoic to Neoproterozoic on the basis of microfossils (Mitrofanov et al., 1981); while Demoux et al. (2009a) inferred a late Mesoproterozoic age from a 1017 Ma maximum depositional zircon age for a quartzite and 1051 Ma zircon age of an associated granite-gneiss. Based on initial Nd mean crustal residence ages of 2700–2500 Ma from carbonaceous phyllites and pelitic schists, the Baidrag basement is considered as a potential source area (Kovalenko et al., 2005; Kozakov et al., 2007). Belts of Paleozoic sediments and volcanic rocks occur in the area of the Burd Gol zone (Demoux et al., 2009a). To the north and structurally below the Burd Gol zone occurs a narrow volcanic-sedimentary unit, where the association of basalt, trachybasalt, andesite, dacite, rhyolite, agglomerate, sandstone and tuff indicates an island arc setting dated at 544 ± 7 Ma (Buchan et al., 2001, 2002; Jian et al., 2010; Kröner et al., 2011).

The Bayankhongor zone contains a central ophiolite mélange (Buchan et al., 2001), with ultramafic cumulates, gabbros, sheeted dikes, pillow lavas, subordinate cherts and limestones, tectonically dismembered within a serpentinite matrix. The ophiolite formation is determined by zircon ages of anorthosite at 665 ± 15 Ma

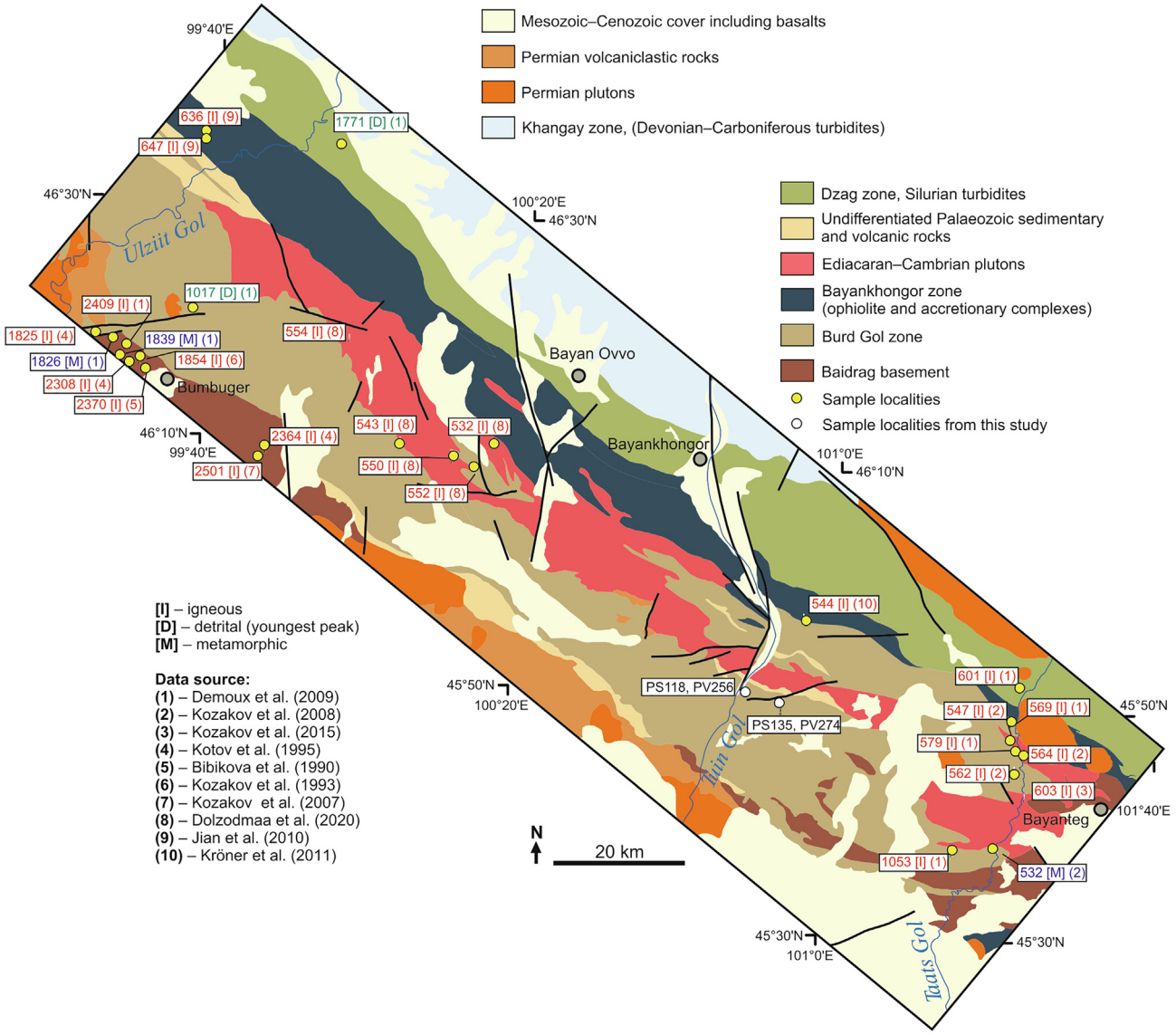

Fig. 2. Simplified geological map of the northeastern margin of the Baidrag block (modified after Tomurtogoo et al., 1998; Demoux et al., 2009a) with compilation of Precambrian geochronological data. Locations of studied samples are indicated.

(Kovach et al., 2005) or 655 ± 4 Ma (Jian et al., 2010), gabbro at ca. 647 Ma and plagiogranite at 636 ± 6 Ma (Jian et al., 2010). Separated by NE verging thrusts, to the south occurs a mélange of metapelitic matrix with lenses of volcanogenic rocks, gabbro, dolerite and pillow lavas, while to the north, a mélange consists of low-grade phyllite with black shale and metasandstone matrix with lenses of Cambrian radiolarian chert, acid volcanics and basalt (Buchan et al., 2001; Tomurtogoo, 2002; Osozawa et al., 2008). The ophiolite is intruded by a syenite porphyry dated at 523 ± 2 Ma (Jian et al., 2010) and the tectonic contact of the central and southern mélange is stitched by an undeformed pluton dated to 545 ± 2 Ma and 539 ± 1 Ma (Buchan et al., 2002).

The Silurian Dzag zone consists of lower greenschist facies pelitic to psammitic rocks with rare limestone and subordinate mafic detritus (Vonesenskaya et al., 1992; Jahn et al., 2004; Osozawa et al., 2008). The sequence is interpreted as turbidites deposited on a passive continental margin (Buchan et al., 2001; Osozawa et al., 2008) as indicated by the dominance of 2140–1770 Ma detrital zircons (Demoux et al., 2009a). Sedimentation age is deduced from a 445 ± 6 Ma maximum depositional age (Kröner et al., 2011). Metamorphic white micas were dated at 454 ± 9 Ma, 447 ± 9 Ma (K-Ar; Kurimoto et al., 1998) and 395 ± 20 Ma (K-Ar; Teraoka et al., 1996).

The Devonian–Carboniferous Khangay zone consists of a turbiditic sequence formed by unmetamorphosed folded sandstone-mudstone with rare chert (Kelty et al., 2008; Osozawa et al., 2008). Late Archean to early Neoproterozoic detrital zircons suggest it was sourced from the Precambrian basement (Kelty et al., 2008). This sedimentary sequence is intruded by early Permian to late Triassic granitoids without signs of deformation (Takahashi et al., 2000; Jahn et al., 2004; Orolmaa et al., 2008; Yarmolyuk et al., 2008; Dolzodmaa et al., 2020).

2.2. Previous metamorphic and geochronological studies of the Burd Gol zone

Increasing metamorphic grade from south to north from biotite, through garnet to staurolite zone was described along the Ulziit Gol transect (Fig. 2) by Buchan et al. (2001). Kozakov et al. (2012) reported a northward increase in metamorphism up to

kyanite–sillimanite zone involving a belt of kyanite–staurolite schists between the Ulziit Gol and the Tuin Gol valleys and estimated *P-T* conditions to be 570–620 °C and 8–10 kbar (Ulziit Gol, Fig. 2) and 600–650 °C and 7–8 kbar (Tuin Gol, Fig. 2). Along the Taats Gol transect, rocks are metamorphosed at amphibolite-facies conditions in the south and reach conditions of partial melting in the north, in particular north of the Ediacaran pluton (Demoux et al., 2009a). Here, Kozakov et al. (2012) described early kyanite- and staurolite-bearing assemblages followed by andalusite-, sillimanite- and cordierite-bearing assemblages.

The age of metamorphism is inferred mainly from zircon U–Pb crystallization ages of Ediacaran–Cambrian intrusions (Kozakov et al., 2006, 2008, 2012; Demoux et al., 2009a). They exhibit in places syntectonic features, such as a kyanite-bearing granitic vein (562 ± 2 Ma, Kozakov et al., 2006), or a foliated granodiorite and granosyenite (547 ± 4 Ma, 564 ± 5 Ma, Kozakov et al., 2006, 2008). In the southern part of the Taats Gol transect a garnet-bearing metagranite interlayered with the surrounding metasediments (532 ± 9 Ma, Kozakov et al., 2008) and a medium-grained syntectonic granite vein (519 ± 9 Ma, Demoux et al., 2009a) were dated.

Kozakov et al. (2012) suggested the time span of 580–565 Ma for the kyanite–staurolite phase of metamorphism, based on zircon ages from a 579 ± 7 Ma quartz diorite and ca. 565 Ma granite (Demoux et al., 2009a). The lower age boundary for the andalusite–cordierite phase of metamorphism observed in the Taats Gol transect was estimated to 542 Ma (Kozakov et al., 2012), supported by the granitoid emplacement ages of ca. 547 Ma for the granitoids which exhibit D2 deformation, and 542 ± 2 Ma for the granitoid that crosscuts D2 deformation zones. Late Neoproterozoic to Cambrian age of metamorphism is also supported by a $^{40}Ar/^{39}Ar$ biotite age of 533 ± 3 Ma from a biotite–garnet gneiss from the SE part of the unit (Höck et al., 2000). However, much older K–Ar age of metamorphic white mica of 699 ± 35 Ma from black schists was reported by Teraoka et al. (1996) from the NW part of the belt.

3. Geology of the Tuin Gol transect

In the south, the transect starts with a metasedimentary sequence composed of sandstone, grey (±garnet) phyllite interlayered with quartzite and fine-grained marble. To the north, the rocks become coarser-grained, and involve (±garnet) micaschist, (±garnet) amphibolite, metasandstone, metagreywacke, quartzite and marble. Towards the Ediacaran pluton, the metasediments in places contain staurolite, kyanite, sillimanite, and locally have migmatitic appearance. At the southern boundary of the Ediacaran pluton occurs a sequence of conglomerate, sandstone and limestone of presumably Permian age, and another belt of Paleozoic flysh-like sequence of sandstone, siltstone, phyllite and limestone with crinoids and ichnofossils, metamorphosed at subgreenschist facies. North of the Ediacaran pluton crops out a migmatitic complex of (±garnet ± sillimanite) paragneiss and (±garnet) amphibolite. This is followed by a complex of granitoids, amphibole-bearing gabbro comingled with tonalite, with subordinate (±garnet ± sillimanite) migmatitic paragneiss, augengneiss and ultrabasic rocks.

The macroscopic observations of index minerals in Al-rich metasediments from south to north involve progressive appearance of biotite, garnet, staurolite, kyanite and sillimanite in schists and gneiss, and thus give an impression that the degree of metamorphism generally increases to the north. All the lithologies are locally affected by greenschist-facies retrogression. The dominant structure is a NW–SE trending steep foliation that reworks earlier metamorphic fabrics, preserved in the form of open to isoclinal folds. Numerous granitic to pegmatitic dykes crosscut the migmatitic complex and exhibit syn- to post-tectonic relationships with respect to the main steep fabric.

3.1. Sample localities

The studied rocks occur south of the Ediacaran pluton. Locality PV274-PS135 (Figs. 2 and 3a, b) is formed by a dark garnet–biotite gneiss with macroscopically visible elongated kyanite (up to 0.5 cm in size), resembling sillimanite. It contains numerous feldspar porphyroblasts and polymineralic leucosomes. Metamorphic foliation is dipping under moderate to shallow angles to the west and contains isoclinal rootless folds of leucosomes.

Localities PS118 and PV256 (Figs. 2 and 3c, d) are several tens of meters apart, both located in a series of outcrops dominated by alternating metapelitic and metapsammitic layers, and locally with up to 1 m thick quartzite. The metapelitic layers are transformed to garnet–staurolite micaschist and the metapsammitic layers contain garnet. The macroscopically visible garnet and staurolite are up to 1 cm and 2 cm in size, respectively. A shallow-dipping metamorphic foliation is folded by steep, open to isoclinal folds, leading locally to transposition into a moderately to steeply SW-dipping cleavage.

4. Petrography and mineral chemistry

4.1. Sample selection and analytical procedure

In an attempt to constrain the Neoproterozoic *P-T-t* paths, we focus only on three localities that revealed Neoproterozoic metamorphic ages, a locality of Grt-Sil-Ky gneiss PV274, and two localities of garnet-staurolite schist PS118 and PV256. Mineral analyses and compositional maps were performed on an electron probe microanalyser (EPMA) with field emission gun electron source JXA-8530F by JEOL (Charles University, Czech Republic), with focused beam mode (15 kV, 30nA) for garnet and staurolite, defocused beam to 5 μm (15 kV, 20nA) for micas and feldspars, and compositional mapping was done with 20 kV and 80nA. Representative analyses are summarized in Table 1. Petrography and garnet zoning are presented in Figs. 4–6. In the text, we use "=>" for mineral compositional trends, while "–" designates a range of mineral compositions; p.f.u. = per formula unit.

4.2. Grt-Sil-Ky gneiss (PV274B)

Grt-Sil-Ky gneiss is composed of garnet, sillimanite, kyanite, biotite, muscovite, plagioclase, K-feldspar, quartz and accessory ilmenite, rutile, tourmaline, zircon and monazite (Fig. 4). It is dominated by a mica-rich matrix and contains bands and lenses of leucosomes composed predominantly of K-feldspar, plagioclase and quartz (Fig. 3b and Fig. 4a). The kyanite and sillimanite occurrences were confirmed by electron-backscattered diffraction (EBSD) analysis. Garnet (up to 0.5 cm) shows commonly lobate boundaries, with apophyses protruding to the matrix. The apophyses have in places numerous small aligned inclusions mostly of quartz, texturally different from the garnet core and in places near the garnet rim an aligned string of inclusions separating the garnet core from rim is observed (Fig. 4b, e and f). Where this textural difference is obvious we assign them as garnet1 and garnet2 (Fig. 4b and f). Garnet contains inclusions of sillimanite, kyanite, biotite, ilmenite, rutile, quartz, plagioclase and monazite. Apart from quartz and plagioclase, the distribution of the inclusions of index minerals shows zoning from core to rim: the inner core includes biotite and ilmenite, the outer core includes sillimanite, biotite and ilmenite, and the very rim and garnet apophyses include sillimanite, kyanite, biotite, ilmenite and rutile (Fig. 4). EBSD analysis in thin-section

Table 1
Representative analyses of (a) garnet and staurolite, (b) muscovite, biotite, plagioclase, K-feldspar. Alm = Fe/(Ca + Fe + Mg + Mn), prp = Mg/(Ca + Fe + Mg + Mn), grs = Ca/(Ca + Fe + Mg + Mn), sps = Mn/(Ca + Fe + Mg + Mn), X_{Fe} = Fe/(Fe + Mg); an = Ca/(Na + Ca + K), ab = Na/(Na + Ca + K), or = K/(Na + Ca + K). b.d. = below detection limit, concentration lower than the value of the 2σ standard deviation. c = core, r = rim.

Rock type	Grt-Sil-Ky gneiss				Grt-St schist				Grt-St schist				Grt-St schist			
Sample	PV274B2	PV274B2	PV274B2	PV274B2	PS118C	PS118C	PS118C	PS118C	PV256B	PV256B	PV256B	PV256B	PS118C	PS118C	PV256B	PV256B
Mineral	Grt	Grt	Grt	Grt	Grt	Grt	Grt	Grt	Grt	Grt	Grt	Grt	St	St	St	St
Position	Grt1-c	Grt1-r	Grt1-r	Grt2-c	Grt1-c	Grt1-r	Grt2-c	Grt2-r	Grt1-c	Grt1-r	Grt2-c	Grt2-r				
Analysis	p26-045	p26-007	p24-07	p25-014	227	241	244	251	134	122	175	187	290	41	167	164
SiO_2	37.61	37.82	37.86	37.64	36.29	36.52	36.58	36.45	36.01	35.85	36.29	36.27	26.78	25.30	25.81	25.85
TiO_2	0.20	0.19	0.21	0.12	0.03	0.00	0.12	0.04	0.01	0.00	0.08	0.02	0.46	0.33	0.35	0.47
Cr_2O_3	0.02	0.01	0.00	0.01	0.03	0.01	0.01	0.02	0.03	0.00	0.01	0.02	0.04	0.03	0.02	0.03
Al_2O_3	20.22	20.69	20.82	20.68	20.44	20.45	20.60	20.57	20.41	20.60	20.63	20.66	53.19	55.41	54.60	55.29
FeO	32.69	34.77	35.49	35.88	32.46	36.24	34.53	35.76	32.29	36.26	34.44	36.22	13.43	13.43	13.33	12.71
MnO	6.26	3.55	2.74	2.62	5.97	2.33	0.77	0.26	5.64	2.06	0.62	0.24	0.03	0.03	0.02	0.01
MgO	2.72	2.94	2.89	2.62	1.62	1.86	1.57	1.92	1.78	2.04	1.79	2.10	1.32	0.80	1.31	0.96
CaO	0.61	0.65	0.69	1.11	1.39	1.38	4.64	3.24	1.33	1.17	4.89	2.84	0.00	0.01	0.01	0.01
Na_2O	0.01	0.01	0.01	0.01	0.01	0.02	0.01	0.01	0.02	0.01	0.01	0.01	0.03	0.02	0.00	0.00
K_2O	0	0	0	0	0	0	0.01	0	0	0	0	0	0.00	0.02	0.00	0.00
P_2O_5	0.00	0.05	0.05	0.02	0.00	0.00	0.02	0.04	0.03	0.02	0.00	0.00	b.d.	b.d.	b.d.	b.d.
ZnO	b.d.	b.d.	b.d.	b.d.	b.d.	b.d.	b.d.	b.d.	b.d.	b.d.	b.d.	b.d.	1.03	0.73	0.55	0.64
Total	100.34	100.67	100.75	100.71	98.26	98.81	98.86	98.29	97.68	98.01	98.76	98.37	96.31	96.12	96.01	95.95
Cations	8.00	8.00	8.00	8.00	8.00	8.00	8.00	8.00	8.00	8.00	8.00	8.00	15.00	15.00	15.00	15.00
Si	3.04	3.04	3.04	3.03	3.01	3.01	2.99	3.00	3.00	2.97	2.96	2.98	3.87	3.65	3.81	3.87
Ti	0.01	0.01	0.01	0.01	0.00	0.00	0.01	0.00	0.00	0.00	0.00	0.00	0.05	0.04	0.04	0.06
Cr	0.00	0.00	0.00	0.00	0.00	0.00	0.00	0.00	0.00	0.00	0.00	0.00	0.00	0.00	0.00	0.01
Al	1.93	1.96	1.97	1.96	2.00	1.98	1.99	1.99	2.00	2.01	1.99	2.00	9.05	9.42	9.19	9.17
Fe^{3+}	0.00	0.00	0.00	0.00	0.00	0.01	0.01	0.00	0.00	0.04	0.07	0.03	0.00	0.00	0.00	0.00
Fe^{2+}	2.21	2.34	2.38	2.41	2.25	2.49	2.35	2.46	2.25	2.47	2.28	2.46	1.62	1.62	1.60	1.65
Mn	0.43	0.24	0.19	0.18	0.42	0.16	0.05	0.02	0.40	0.14	0.04	0.02	0.00	0.00	0.00	0.01
Mg	0.33	0.35	0.35	0.31	0.20	0.23	0.19	0.24	0.22	0.25	0.22	0.26	0.28	0.17	0.29	0.18
Ca	0.05	0.06	0.06	0.10	0.12	0.12	0.41	0.29	0.12	0.10	0.43	0.25	0.00	0.00	0.00	0.00
Na	0.00	0.00	0.00	0.00	0.00	0.00	0.00	0.00	0.00	0.00	0.00	0.00	0.01	0.01	0.00	0.00
K	0.00	0.00	0.00	0.00	0.00	0.00	0.00	0.00	0.00	0.00	0.00	0.00	0.00	0.00	0.00	0.00
P	0.00	0.00	0.00	0.00	0.00	0.00	0.00	0.00	0.00	0.00	0.00	0.00	b.d.	b.d.	b.d.	b.d.
Zn	b.d.	b.d.	b.d.	b.d.	b.d.	b.d.	b.d.	b.d.	b.d.	b.d.	b.d.	b.d.	0.11	0.08	0.05	0.06
grs	0.02	0.02	0.02	0.03	0.04	0.04	0.13	0.10	0.04	0.03	0.14	0.08				
alm	0.73	0.78	0.80	0.80	0.75	0.83	0.78	0.82	0.75	0.83	0.77	0.83				
py	0.11	0.12	0.12	0.10	0.07	0.08	0.06	0.08	0.07	0.08	0.07	0.09				
sps	0.14	0.08	0.06	0.06	0.14	0.05	0.02	0.01	0.13	0.05	0.01	0.01				
$X_{Fe(tot)}$	0.87	0.87	0.87	0.88	0.92	0.92	0.93	0.91	0.91	0.91	0.92	0.91	0.85	0.90	0.85	0.90

Rock type	Grt-Sil-Ky gneiss				Grt-St schist						Grt-St schist		
Sample	PV274B	PV274B	PV274B	PV274B	PS118C	PS118C	PS118C	PS118C	PS118C	PS118C	PV256B	PV256B	PV256B
Mineral	Ms	Bt	Ksp	Plg	Ms	Ms	Ms	Bt	Plg	Plg	Ms	Bt	Plg
Position						rim	core						
Analysis	105	100	96	98	91	128	131	127	116	284	189	190	200
SiO_2	44.96	34.66	63.51	63.88	45.41	46.05	45.93	34.68	62.46	64.13	45.50	34.38	62.15
TiO_2	1.01	3.18	0.00	0.00	0.21	0.19	0.16	1.57	0.01	0.00	0.46	1.43	0.01
Al_2O_3	36.17	18.90	19.13	22.61	35.90	35.96	36.79	18.85	23.11	21.45	36.66	18.35	23.21
FeO	1.22	20.68	0.24	0.21	1.90	0.96	0.99	21.29	0.06	0.05	1.06	21.21	0.03
MnO	0.01	0.06	0.00	0.02	0.00	0.00	0.00	0.02	0.00	0.00	0.00	0.02	0.01
MgO	0.65	7.58	0.01	0.00	0.42	0.48	0.37	7.77	0.00	0.00	0.46	8.27	0.00
CaO	0.05	0.01	0.01	2.88	0.00	0.02	0.00	0.05	4.52	2.68	0.01	0.07	4.58
Na_2O	0.44	0.10	1.08	9.53	1.21	1.23	1.77	0.18	8.83	9.61	1.33	0.09	8.71
K_2O	10.35	9.59	14.99	0.15	9.08	8.96	8.23	8.58	0.09	0.04	8.96	8.43	0.07
BaO	0.19	0.08	0.65	0.00	0.18	0.19	0.16	0.04	0.00	0.00	0.23	0.04	0.00
Total	95.05	94.83	99.61	99.27	94.30	94.04	94.39	93.02	99.08	97.94	94.66	92.29	98.75
Cations	7.00	8.00	5.00	5.00	7.00	7.00	7.00	8.00	5.00	5.00	7.00	8.00	5.00
Si	3.01	2.76	2.95	2.84	3.05	3.10	3.07	2.81	2.79	2.89	3.04	2.80	2.79
Ti	0.05	0.19	0.00	0.00	0.01	0.01	0.01	0.10	0.00	0.00	0.02	0.09	0.00
Al	2.85	1.77	1.05	1.18	2.84	2.85	2.90	1.80	1.22	1.14	2.89	1.76	1.23
Fe^{3+}	0.00	0.00	0.01	0.00	0.00	0.00	0.00	0.00	0.00	0.00	0.00	0.00	0.00
Fe^{2+}	0.07	1.38	0.00	0.01	0.11	0.05	0.06	1.44	0.00	0.00	0.06	1.44	0.00
Mn	0.00	0.00	0.00	0.00	0.00	0.00	0.00	0.00	0.00	0.00	0.00	0.00	0.00
Mg	0.07	0.90	0.00	0.00	0.04	0.05	0.04	0.94	0.00	0.00	0.05	1.00	0.00
Ca	0.00	0.00	0.00	0.14	0.00	0.00	0.00	0.00	0.22	0.13	0.00	0.01	0.22
Na	0.06	0.02	0.10	0.82	0.16	0.16	0.23	0.03	0.77	0.84	0.17	0.01	0.76
K	0.88	0.97	0.89	0.01	0.78	0.77	0.70	0.89	0.00	0.00	0.76	0.88	0.00
Ba	0.01	0.00	0.01	0.00	0.01	0.01	0.00	0.00	0.00	0.00	0.01	0.00	0.00
X_{Fe}	0.51	0.60			0.72	0.53	0.60	0.61			0.56	0.59	
an			0.00	0.14					0.22	0.13			0.22
ab			0.10	0.85					0.78	0.86			0.77
or			0.90	0.01					0.00	0.00			0.00

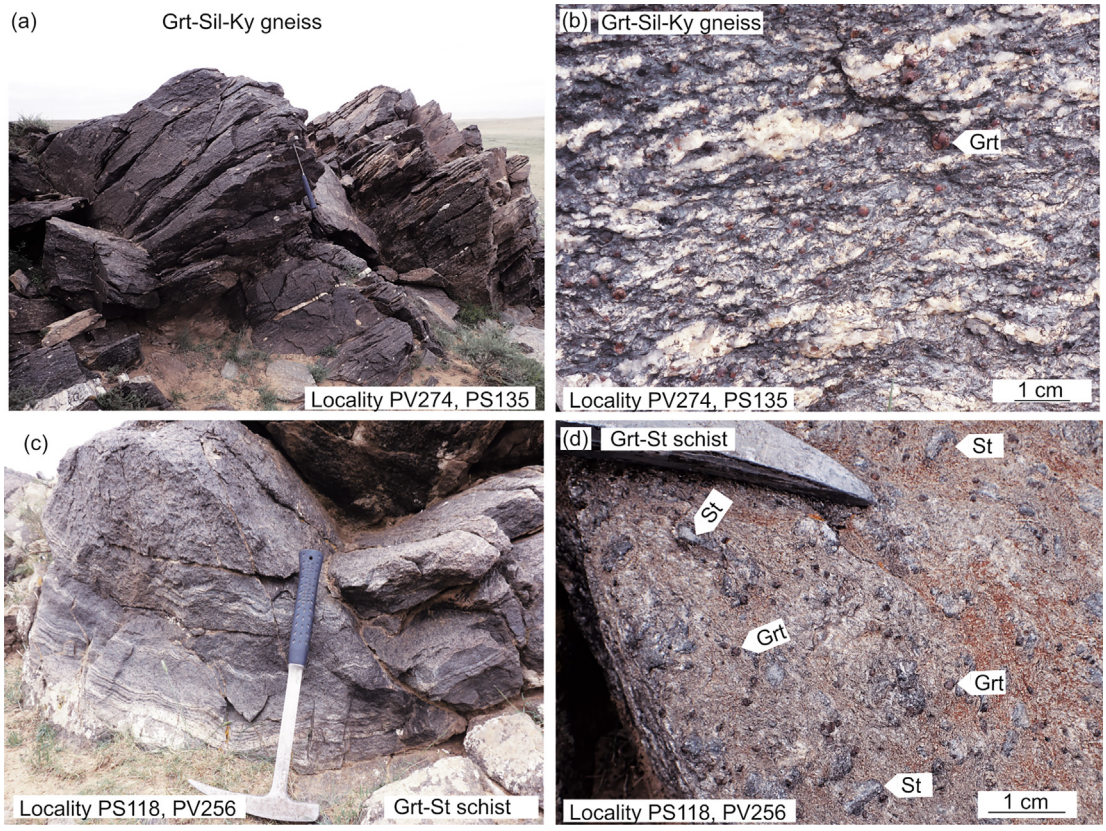

Fig. 3. Field photographs illustrate the studied rock types. (a, b) Grt-Sil-Ky gneiss with bands and lenses of leucosomes, (c, d) Grt-St schist.

and XRD analysis on mineral separates from the matrix did not detect sillimanite in the matrix, all Al_2SiO_5 in the matrix was kyanite. Apart from kyanite included in the garnet rim and garnet apophyses (Fig. 4c–f), numerous kyanite grains (up to 0.5 cm in size) are aligned mostly in biotite-rich layers, and some grains occur also in leucocratic layers (Fig. 4b, d and e). Biotite dominates the mica-rich layers, and it is associated with numerous grains of kyanite. In places muscovite is aligned with biotite and also contains kyanite inclusions (Fig. 4b and d), suggesting crystallization of muscovite at the expense of, and after kyanite. Occasional muscovite appearing in the garnet rim (Fig. 4d) is connected by cracks to the matrix and is therefore interpreted as a late phase. The succession of index mineral crystallization from these observations is core of garnet1 with Bt-Ilm, outer core of garnet1 with Sil-Bt-Ilm, garnet2 with Ky-Rt and the matrix with Ky-Ms-Rt-Ilm.

Some garnet grains show strong zoning marked by a continuous decrease in spessartine and an increase in almandine from core towards rim, while grossular, pyrope and X_{Fe} are almost constant, and followed by a minor increase in spessartine, almandine, grossular and X_{Fe}, and a decrease in pyrope, at the very rim (Fig. 6a, profile p26–27; $grs_{0.01=>0.02}$, $alm_{0.73\ =>\ 0.78,}$ $prp_{0.11\ =>\ 0.12}$, $sps_{0.14\ =>\ 0.08}$, $X_{Fe\ 0.87\ =>\ 0.89}$). Other garnet grains show similar type of zoning, but less pronounced, and in some garnet2 apophyses this zoning is followed by a small, but systematic increase in grossular, almandine and X_{Fe}, and a continuous decrease in pyrope and spessartine (Fig. 6b) (profile p24–25; $grs_{0.02\ =>\ 0.02\ =>\ 0.04}$, $alm_{0.78\ =>\ 0.79\ =>\ 0.80,}$ $prp_{0.11\ =>\ 0.12\ =>\ 0.10}$, $sps_{0.09\ =>\ 0.06\ =>\ 0.05}$, $X_{Fe\ 0.87\ =>\ 0.88\ =>\ 0.89}$). Plagioclase is oligoclase ($an_{0.13-0.15}$ $ab_{0.86-0.84}$ $or_{0.01}$), K-feldspar contains 9%–11% of albite. Muscovite has Si = 3.00–3.04 p.f.u. and Na = 0.05–0.06 p.f.u. Biotite has X_{Fe} = 0.54–0.60 and Ti = 0.19–0.24 p.f.u.

4.3. Grt-St schists (PS118C and PV256B)

Both samples are composed of garnet, staurolite, biotite, muscovite, plagioclase, quartz, chlorite, and accessory ilmenite, tourmaline, zircon and monazite (Fig. 5). Garnet (up to 3 mm) is included in staurolite and also occurs in the matrix. The garnet included in staurolite tends to be euhedral, while garnet in the matrix tends to have a euhedral to subhedral core surrounded by highly irregular anhedral garnet with apophyses protruding to the matrix (Fig. 5a). We interpret these textural differences as a result of two stages of garnet growth, assigned here as garnet1 and garnet2. Some garnet grains have rare inclusions while other grains contain numerous inclusions of quartz and ilmenite. The inclusions tend to be strongly oriented and form inclusion trails in the euhedral garnet, while they tend to be irregular in the subhedral garnet. Staurolite (up to 1 cm) tends to include garnet1, numerous oriented and elongated quartz and rare ilmenite. When garnet1 is included in staurolite, and both contain inclusion trails, these inclusion trails are parallel with the crystal elongation of staurolite, indicating crystallization in the same foliation (Fig. 5a and c). The matrix contains layers dominated by muscovite and biotite, alternating with layers dominated by plagioclase and quartz with some biotite and subordinate muscovite. Chlorite locally occurs in the vicinity of staurolite and garnet (Fig. 5b), and some biotites show transformation to chlorite. Staurolite is in places surrounded by an aggregate dominated by fine-grained muscovite, chlorite and ilmenite (Fig. 5b), interpreted as a partial pseudomorph after staurolite. From the textural relations the inferred succession of crystallization of index minerals is as follows: garnet1, staurolite, followed by garnet2, with stable muscovite, biotite and ilmenite. This is followed by late crystallization of chlorite.

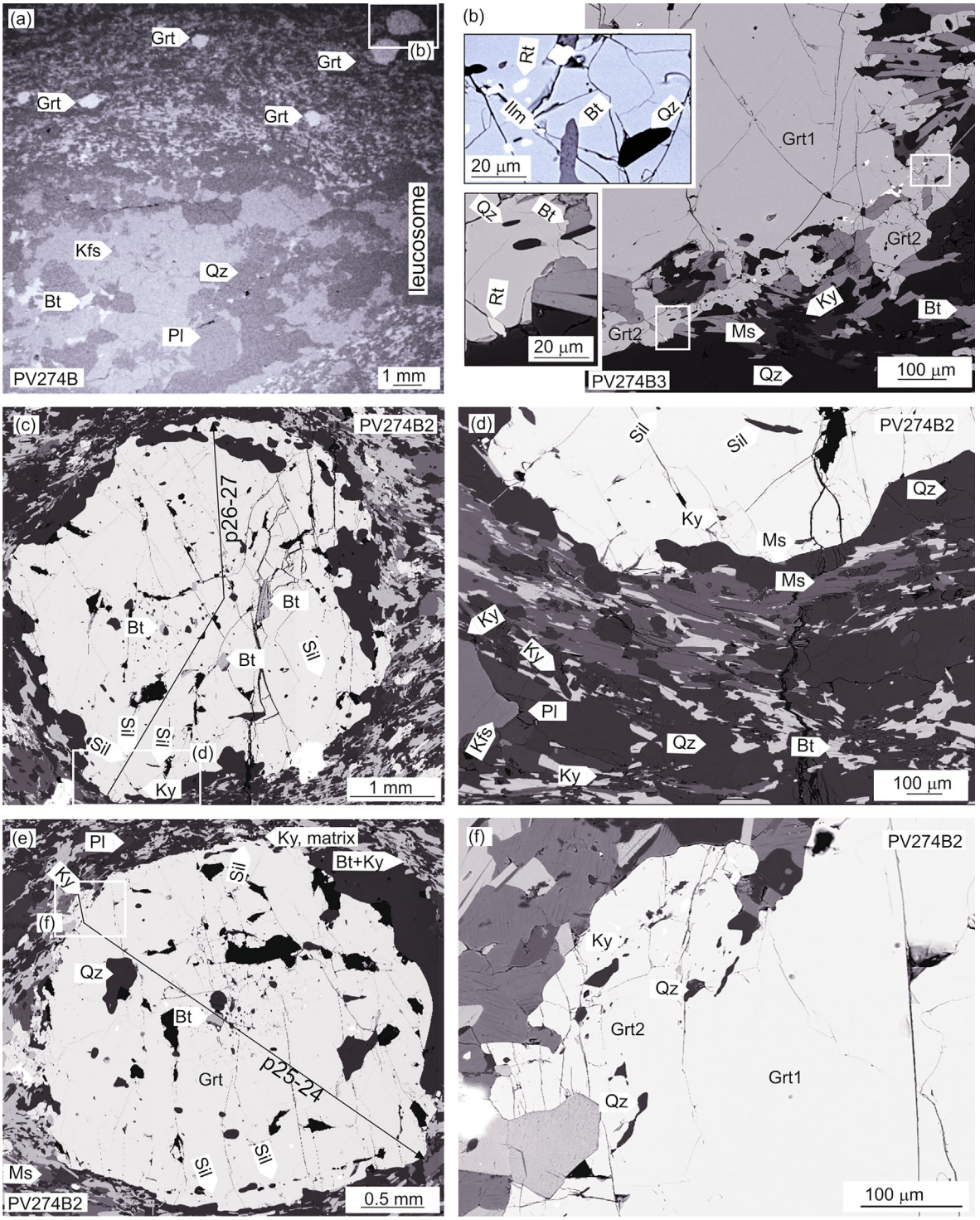

Fig. 4. BSE images of Grt-Sil-Ky gneiss sample PV274B showing main petrographic features and crystallization succession (kyanite and sillimanite are confirmed by EBSD analyses). (a) Coarse-grained leucosome lens composed of K-feldspar, plagioclase, quartz and biotite, in a finer-grained matrix. (b) Garnet in a matrix composed of kyanite, biotite, muscovite, plagioclase, K-feldspar, quartz. Garnet shows inclusion-rich apophyses of garnet2 around garnet1. Indicated insets show details of inclusions of rutile, biotite and quartz in garnet2. (c) Inclusions of index minerals from core to rim in garnet show biotite in the core, followed by a zone with sillimanite, and kyanite at the rim. A rectangle indicates a detail portrayed in (d). Black line indicates position of chemical profile. (d) Detail of sillimanite and kyanite inclusions in garnet. Muscovite in garnet is connected with cracks to matrix. Matrix is composed of kyanite, biotite, muscovite, plagioclase, K-feldspar, quartz. (e) Garnet with large core of garnet1, and irregular apophyses assigned as garnet2. The boundary between garnet1 and garnet2 is not abrupt, it is in places marked by aligned inclusions of quartz. Garnet2 tends to contain numerous inclusions that are smaller compared to those in garnet1. Indicated are inclusions of sillimanite at the boundary of garnet1 and garnet2, and a rectangle marks an area with kyanite detailed in (f). Black line indicates position of chemical profile. (f) Kyanite and numerous small elongated quartz inclusions in garnet2.

In sample PS118C, garnet1 is characterized by low and nearly constant grossular content, nearly constant or slight increase in pyrope, strong decrease in spessartine and increase in almandine from core to rim (Fig. 6d, garnet1 in profile p55–56; $grs_{0.04}$, $alm_{0.75 \Rightarrow 0.83}$, $prp_{0.07 \Rightarrow 0.10}$, $sps_{0.14 \Rightarrow 0.05}$, $X_{Fe\ 0.91-0.92}$). Some garnet1 grains show less pronounced zoning (Fig. 6c), with lower

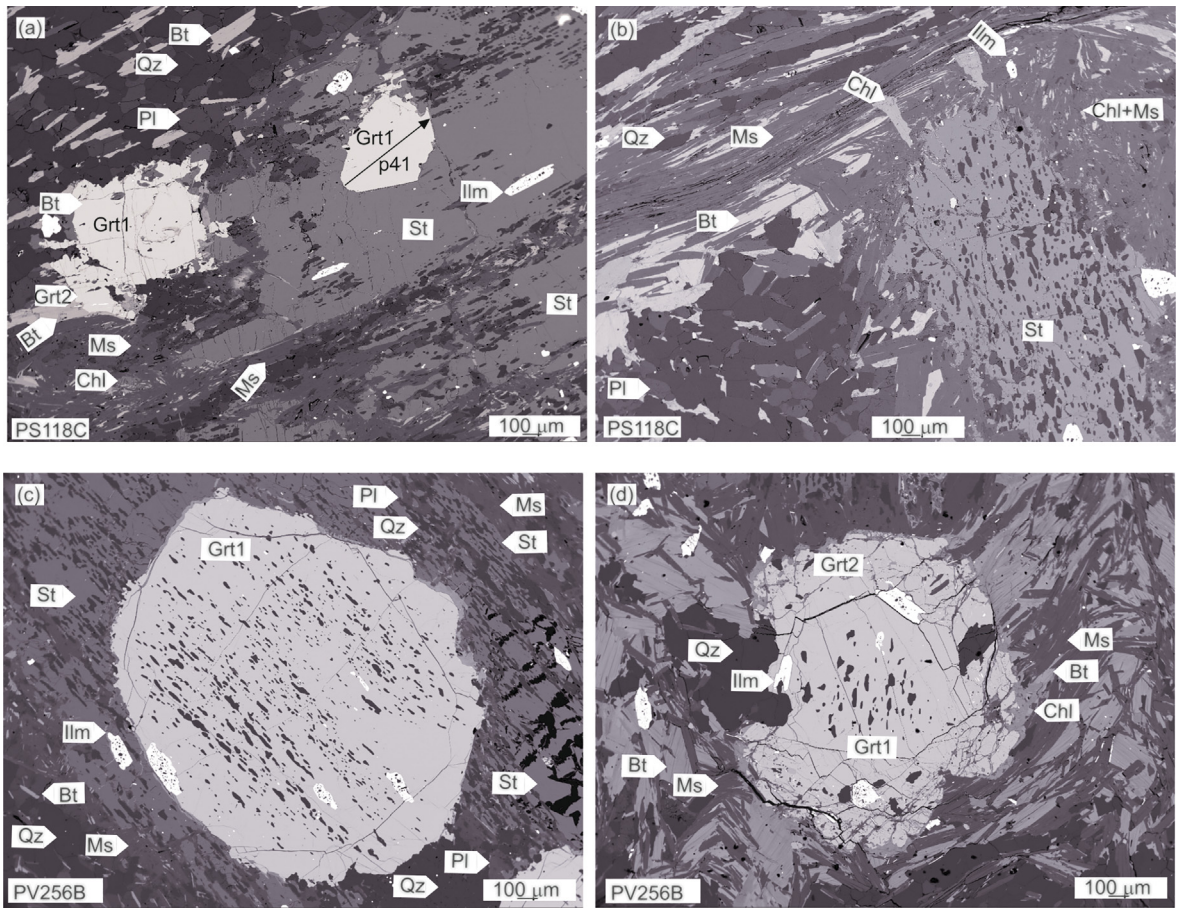

Fig. 5. BSE images of garnet-staurolite schists, showing crystallization succession. (a) Garnet1 included in staurolite shows some euhedral boundaries towards staurolite and some apophyses connected to the matrix; garnet in the matrix shows a core formed by garnet1 and apophyses of garnet2, inclusion trails in staurolite are parallel to the matrix, sample PS118C. (b) Staurolite in a matrix of biotite, muscovite, quartz and plagioclase, inclusion trails in staurolite are at high angle to the matrix, sample PS118C. (c) Garnet included in staurolite, both showing inclusion trails parallel to the matrix, sample PV256B. (d) Garnet in a folded matrix. Garnet shows a core of garnet1 with inclusion trails at high angle to the matrix, and an irregular rim of garnet2, sample PV256B.

spessartine and higher almandine in the core compared to garnet1 profile p55–56 (Fig. 6d), and this is interpreted as chemical characteristics of grains not cut through their core. The limit between garnet1 and garnet2 is marked mainly by an abrupt increase in grossular from 0.04 to 0.13 (Fig. 6d and e). Anhedral garnet2 is characterized by relatively high but decreasing grossular content, low and decreasing spessartine, and increasing almandine and pyrope contents (Fig. 6d and e), e.g. garnet2 in profile p55–56; $grs_{0.14 \Rightarrow 0.10}$, $alm_{0.78 \Rightarrow 0.83}$, $prp_{0.06 \Rightarrow 0.08}$, $sps_{0.02 \Rightarrow 0.01}$, $X_{Fe\ 0.91-0.93}$). Staurolite contains Ti = 0.03–0.06 p.f.u., Zn = 0.05–0.12 p.f.u. and Mn = 0.00–0.01 p.f.u., and X_{Fe} ranges 0.84–0.90. Plagioclase is oligoclase ($an_{0.13-0.22}$ $ab_{0.86-0.78}$ $or_{0.00-0.01}$), muscovite has Si = 3.05–3.10 p.f.u. and Na = 0.15–0.19 p.f.u., biotite has X_{Fe} = 0.56–0.61 and Ti = 0.07–0.10 p.f.u.

5. Mineral equilibria modelling

5.1. Calculation methods

Calculations were done in the system MnO–Na_2O–CaO–K_2O–FeO–MgO–Al_2O_3–SiO_2–H_2O–TiO_2–O (MnNCKFMASHTO) using THERMOCALC 3.50beta, dataset 6.2 (Holland and Powell, 2011, 6th February 2012 upgrade), and activity models for plagioclase and K-feldspar from Holland et al. (2021), muscovite, staurolite and melt from White et al. (2014a) and garnet, biotite, cordierite and chlorite from White et al. (2014b). The whole rock compositions acquired by quantitative analysis of representative areas of the thin-sections using a scanning electron microscope (SEM) (e.g. Broussolle et al., 2015; Jiang et al., 2015) are normalized to 100 mol% and presented in diagrams (Figs. 7 and 8). The whole rock composition used for modelling of Grt-Sil-Ky gneiss includes both the mica-rich layers and quartzo-feldspathic layers/lenses, as the quartzo-feldspathic layers/lenses texturally appear to be an integral part of the rock and not a result of an externally added melt (Fig. 3b). Fe_2O_3 was set in form of oxygen to O = 0.01, compatible with the observed assemblages without magnetite. Isopleths of pyrope, prp = Mg/(Fe^{2+}+Mg + Ca + Mn), grossular, grs = Ca/(Fe^{2+}+Mg + Ca + Mn), spessartine, sps = Mn/(Fe^{2+}+Mg + Ca + Mn) and staurolite X_{Fe} = FeO/(FeO + MgO) were plotted to study *P-T* conditions of mineral growth. The approaches for how the amount of H_2O, melt, and fractionation calculations were determined, is described separately for the two types of samples below.

5.2. P-T path of Grt-Sil-Ky gneiss PV274B

The reconstruction of a prograde and retrograde *P-T* path for migmatites requires several steps (Štípská et al., 2008): "It involves the determination of H_2O in the final assemblage, consideration of open system behaviour with respect to melt, and modification of the whole-rock composition by adding (or subtracting) melt (White and Powell, 2002). Tracking of the *P-T* path must therefore be undertaken backwards in time, from the matrix assemblage to

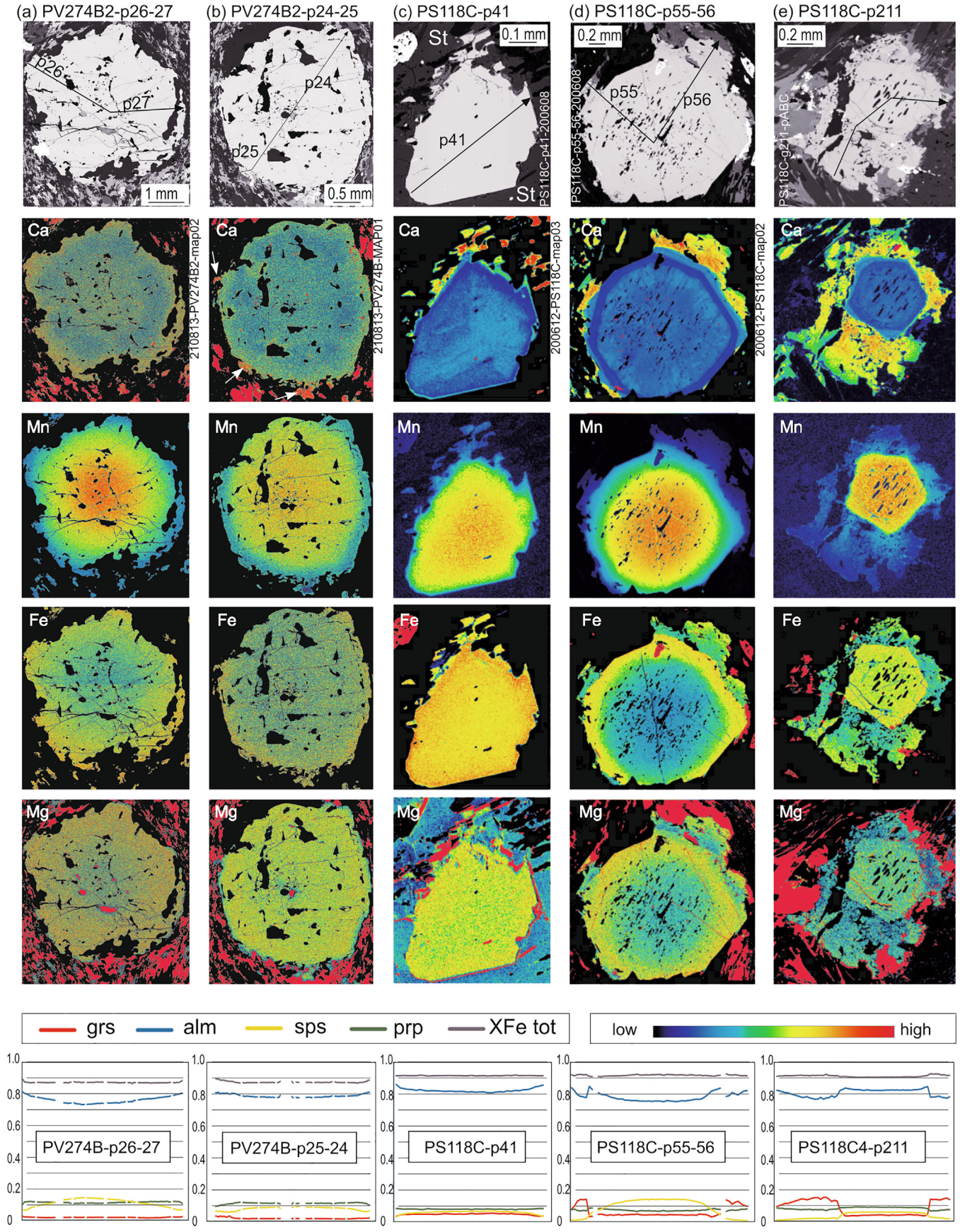
(a) PV274B2-p26-27
(b) PV274B2-p24-25
(c) PS118C-p41
(d) PS118C-p55-56
(e) PS118C-p211
p26
p27
1 mm
p24
p25
0.5 mm
St
0.1 mm
p41
St
PS118C-p41-200608
0.2 mm
p55
p56
PS118C-p55-56-200608
0.2 mm
PS118C-g211-pABC
Ca
210813-PV274B2-map02
Ca
210813-PV274B-MAP01
Ca
200612-PS118C-map03
Ca
200612-PS118C-map02
Ca
Mn
Mn
Mn
Mn
Mn
Fe
Fe
Fe
Fe
Fe
Mg
Mg
Mg
Mg
Mg
grs
alm
sps
prp
XFe tot
low
high
1.0
0.8
0.6
0.4
0.2
0
PV274B-p26-27
PV274B-p25-24
PS118C-p41
PS118C-p55-56
PS118C4-p211

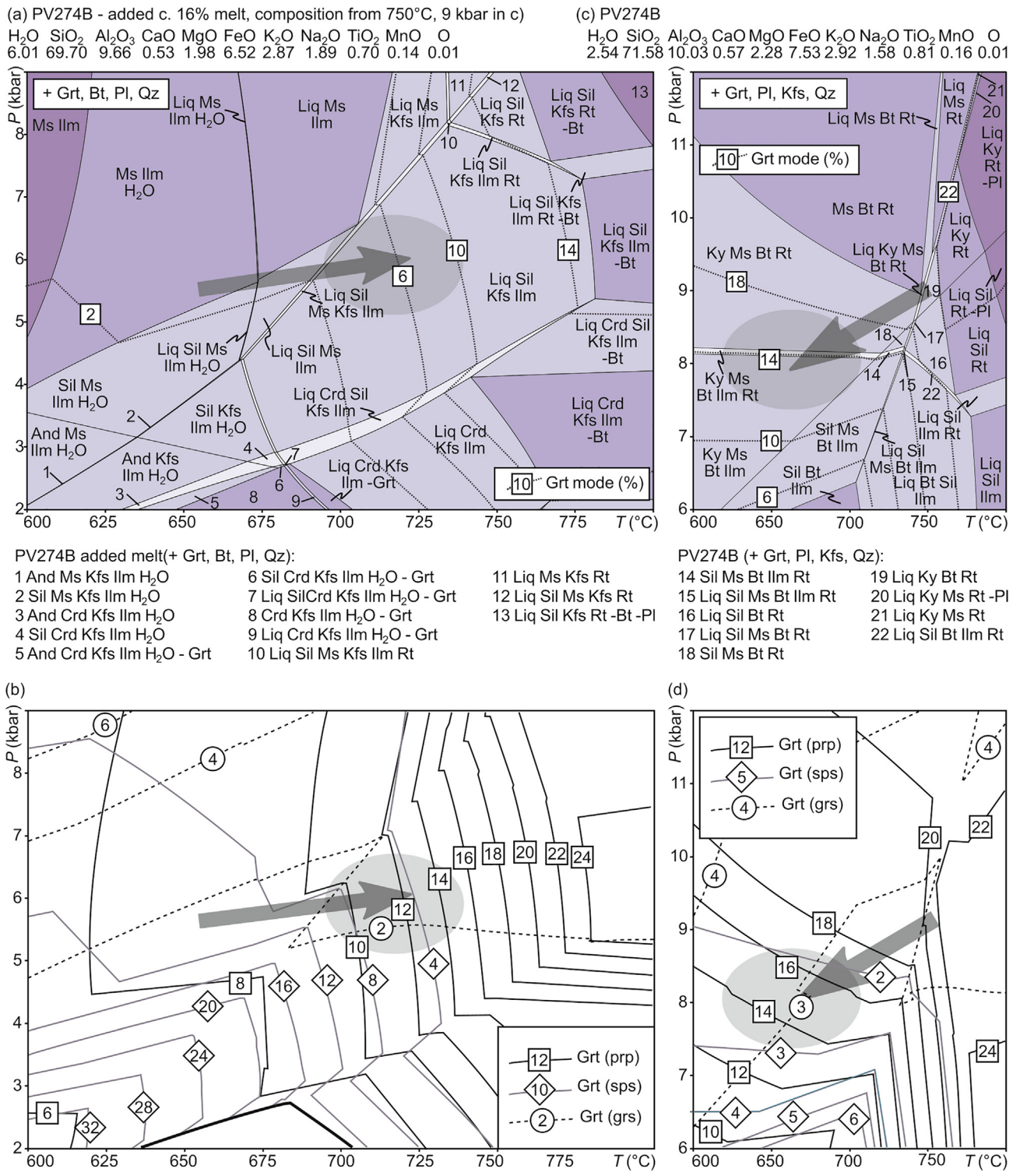

Fig. 7. (a, b) Pseudosection calculated for a whole rock composition with reintegrated melt, Grt-Sil-Ky gneiss sample PV274B, contoured with compositional and modal isopleths of garnet. (c, d) Pseudosection calculated for a whole rock composition contoured with garnet isopleths. The arrows and ellipses indicate the inferred *P-T* conditions, note the different *P-T* scales. For details see text.

Fig. 6. Garnet compositional maps and profiles, (a, b) in sample of Grt-Sil-Ky gneiss, sample PV274B, and (c–e) in sample of Grt-St schist PS118C. (a) Garnet with high-Mn core and low-Mn rim, and with slight increase in Ca at the rim. (e) Garnet with low-Ca garnet1 core shows slight increase in Ca at the rim, and even higher-Ca irregular apophyses of garnet2 (marked with arrows). (c) Garnet included in staurolite shows low-Ca garnet1 with euhedral boundary towards staurolite and few apophyses of high-Ca garnet2 connected to the matrix. (d) Garnet in a matrix, shows a low-Ca core of euhedral garnet1 with strongly zoned Mn, and a sharp boundary with higher-Ca irregular rim of garnet2. (e) Garnet in a matrix shows a low-Ca core of euhedral garnet1, a sharp boundary with higher-Ca irregular rim of garnet2 with numerous small inclusions. (f) Garnet profiles along the black arrows indicated in (a–e).

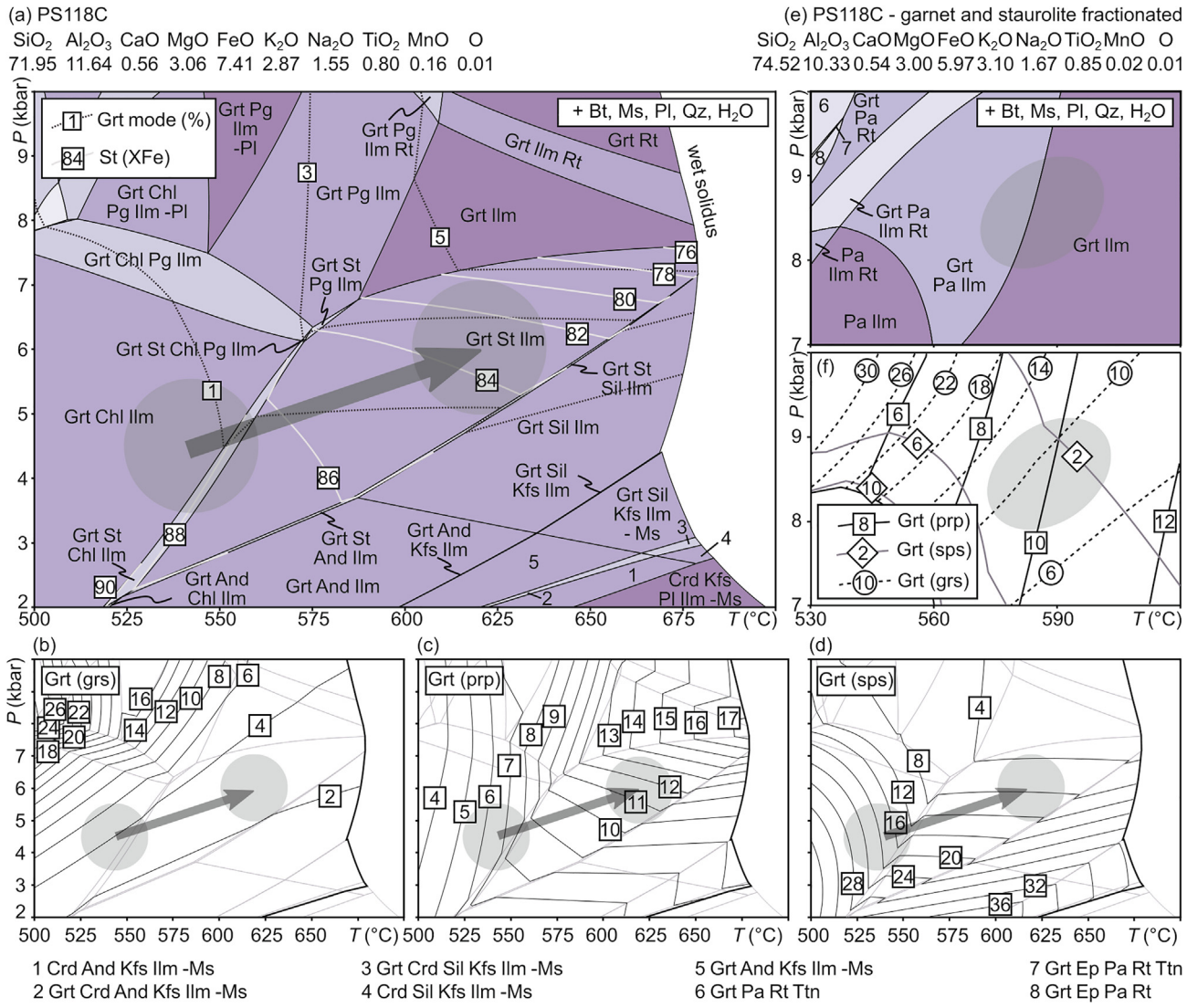

Fig. 8. (a–d) H_2O-saturated pseudosection for sample of Grt-St schist PS118C with calculated mineral compositional and modal isopleths of garnet and staurolite. (e, f) The pseudosection calculated for a fractionated whole rock composition. The arrows and ellipses indicate the inferred *P-T* conditions, note the different *P-T* scales. See text for details.

the early prograde evolution. As the whole-rock composition is expected to change along the *P-T* path via loss of melt and/or H_2O, individual segments of the *P-T* path are modelled in pseudosections calculated for different whole-rock compositions.".

Textural features of the matrix, and the inclusions within the garent2 indicate stability of Grt2-Ky-Rt-bearing mineral assemblage at some point of the *P-T* path. Kyanite grains surrounded by large flakes of muscovite in the matrix then indicate passing to the muscovite stability field. Growth of such muscovite requires aluminosilicate and H_2O, which is typically available at supra-solidus conditions in melt. Because a large quantity of kyanite in the sample is preserved, the amount of H_2O and therefore of the melt itself must have been limited. We searched for the amount of H_2O that allows crystallization of muscovite and preservation of kyanite in a *T*–H_2O section (not shown), and then we used 2.54 mol% of H_2O for the pseudosection calculation (Fig. 7c and d). Such a limited amount of H_2O is explained in migmatites by melt loss (White and Powell, 2002), therefore in order to model the prograde *P-T* path, we reintegrated melt back in to the whole rock composition (Fig. 7a and b). However, even if the calculations are done to track the evolution backwards in time, the diagrams are presented in order as the rock would evolve in time, with an early prograde *P-T* path in Fig. 7a,b and a peak and a retrograde *P-T* path in Fig. 7c,d.

The occurrence of kyanite and rutile inclusions in garnet2 is compatible with peak *P-T* conditions in the field Liq-Grt-Ky-Bt-Pl-Rt (Fig. 7c, d) at ~750 °C and ~9 kbar. The muscovite flakes around kyanite indicate back-crossing of the upper muscovite stability to the field Grt-Ky-Ms-Bt-Pl-Rt, where melt is predicted to be consumed along a narrow temperature interval. The limited amount of H_2O in the calculations, and therefore limited amount of melt are sufficient for conversion of only part of kyanite to muscovite, in accordance with the kyanite presence in the sample. The presence of ilmenite together with rutile in the matrix indicate passing through the calculated field Grt-Ky-Ms-Bt-Pl-Rt-Ilm at ~8 kbar and ~600–700 °C. The peak and retrograde path are inferred mainly based on the evolution of the mineral assemblage. However, even if likely partially reequilibrated by diffusion, as also indicated by the diffuse boundary between garnet1 and garnet2 ($grs_{0.02 \Rightarrow 0.02 \Rightarrow 0.04}$, $alm_{0.78 \Rightarrow 0.79 \Rightarrow 0.80}$, $prp_{0.11 \Rightarrow 0.12 \Rightarrow 0.10}$, $sps_{0.09 \Rightarrow 0.06 \Rightarrow 0.06}$, $X_{Fe\ 0.87 \Rightarrow 0.88 \Rightarrow 0.89}$), this *P-T* path is also compatible with garnet2 composition marked by elevated grossular content (~4%) compared to garent1 (~2%).

In order to model the prograde *P–T* path, we searched for the amount of melt to be reintegrated. The amount of reintegrated melt should lead to the presence of an insignificant amount of H_2O at the wet solidus, because metasediments dehydrate semi-continuously along a prograde *P-T* path (White and Powell, 2002). Reintegration of 16.4 mode% of melt with composition taken from the previously inferred peak at 750 °C and 9 kbar (in mol%: H_2O = 0.602, SiO_2 = 1.272, Al_2O_3 = 0.161, CaO = 0.007, MgO = 0.003, FeO = 0.007, K_2O = 0.057, Na_2O = 0.083), led to calculation of insignificant amount of free H_2O (<0.1 mode%) at the wet solidus (Fig. 7a, b), and the diagram with this amount of reintegrated melt was used to discuss the prograde *P-T* path (Fig. 7a, b). The whole rock composition with the reintegrated melt is supposed to closely approach the original whole rock composition in which the prograde garnet grew (e.g. Štípská et al., 2008). Therefore, an attempt is made to use garnet to constrain the prograde path from inclusion assemblages and from mineral compositions.

The observed succession of crystallization of index minerals from garnet inclusions indicates initial garnet crystallization outside the stability field of sillimanite mostly at subsolidus conditions, likely in the assemblage Grt-Ms-Bt-Ilm-H_2O-Pl-Qz (Fig. 7a). A zone of sillimanite inclusions that are not accompanied by muscovite indicates continuation of garnet growth in the stability of sillimanite and also outside the stability of muscovite, compatible with the calculated Liq-Grt-Sil-Bt-Kfs-Ilm-Pl-Qz field (Fig. 7a). The presence of leucosomes and K-feldspar in the matrix also support the inferred suprasolidus conditions. Garnet modal isopleths indicate garnet growth along such a *P-T* path up to 6 mode% (Fig. 7b). Although the garnet zoning is generally modified by diffusion at suprasolidus conditions, in some cases, the prograde zoning is relatively well preserved despite high grade conditions (e.g. Štípská et al., 2008; Jedlička et al., 2015). Indeed, some of the studied garnets preserve less pronounced prograde zoning, which is interpreted as a result of partial re-equilibration. However, the strong spessartine zoning in some garnets indicates remnants of prograde garnet1 composition ($grs_{0.01=>0.02}$, $alm_{0.73\ =>\ 0.78}$, $prp_{0.11\ =>\ 0.12}$, $sps_{0.14\ =>\ 0.08}$, $X_{Fe\ 0.87\ =>\ 0.89}$) compatible with garnet growth from ~660 °C and ~5.5 kbar to ~720 °C and ~6 kbar, according to plotted garnet isopleths in Fig. 7b. The presence of both sillimanite and kyanite inclusions at the very rim of garnet1, and the occurrence of kyanite and rutile inclusions in garnet2 indicate subsequent increase in pressure, discussed above (Fig. 7c,d).

Continuous melting reactions are inferred according to the modal changes of phases along the *P-T* path in suprasolidus conditions. Along the first part of the prograde *P-T* path, the major melt producing reaction is a muscovite consuming reaction Ms + Pl + Qz + Ilm = Grt + Sil + Liq + Kfs + Bt, followed by a biotite consuming reaction Sil + Qz + Pl + Bt = Grt + Kfs + Liq + Ilm. Along the second part of the *P-T* path with increase in pressure and temperature it is a biotite consuming reaction Sil/Ky + Qz + Pl + Bt = Grt + Kfs + Liq + Ilm/Rt. Garnet formed in the course of such reactions is therefore peritectic.

5.3. P-T path of garnet-staurolite schist PS118C

According to petrological observations, the evolution of this sample occurred under subsolidus conditions, and therefore H_2O was set in excess. Succession of crystallization indicates beginning of garnet1 growth before staurolite, and garnet1 and staurolite growth in the stability of ilmenite. Zoning of garnet1 ($grs_{0.04}$, $alm_{0.75\ =>\ 0.83}$, $prp_{0.07\ =>\ 0.10}$, $sps_{0.14\ =>\ 0.05}$, $X_{Fe\ 0.91-0.92}$) suggests garnet growth from ~530–550 °C and ~4.0–5.0 kbar to ~620 °C and ~6 kbar, compatible with the inferred succession of crystallization (Fig. 8a–d). The *P-T* phase diagram constructed for the fractionated composition is shown in Fig. 8e, f. Subtraction was done via the rbi script close to the peak of the first part of the *P-T* path, at 600 °C and 5.5 kbar (1.8 mode% of garnet with composition in mol%: SiO_2 = 3.000, Al_2O_3 = 0.999, CaO = 0.111, MgO = 0.318, FeO = 2.330, MnO = 0.241, O = 0.001; and 2.2 mode% of staurolite with composition in mol%: H_2O = 2.000, SiO_2 = 7.500, Al_2O_3 = 8.929, MgO = 0.619, FeO = 3.345, TiO_2 = 0.101, MnO = 0.419, O = 0.003). The garnet-in line is shifted to higher pressure and the garnet2 composition ($grs_{0.14\ =>\ 0.10}$, $alm_{0.78\ =>\ 0.83}$, $prp_{0.06\ =>\ 0.08}$, $sps_{0.02\ =>\ 0.01}$, $X_{Fe\ 0.91-0.93}$) is compatible with isopleths at ~570–600 °C and ~8.5 kbar (Fig. 8e, f), indicating a substantial increase in pressure. These conditions occur at the boundary of the stability fields Grt-Bt-Ms-Pg-Ilm-Pl-Ab-Qz and Grt-Bt-Ms-Ilm-Pl-Ab-Qz. The calculated amount of paragonite in the area of the inferred *P-T* conditions is 0.0–1.0 mode%, and therefore paragonite may have been overlooked in the thinsection, for example, it may be present in the form of submicroscopic intergrowths in white mica (e.g. Höck, 1974).

6. Monazite and xenotime geochronology and trace-element chemistry

6.1. Methodology and sample preparation

In order to find a representative number of monazite inclusions in porphyroblasts and from the matrix, we prepared 10 thinsections from samples PV274B, PS118C and PV256B. Before the analysis, monazite and xenotime grains were documented in backscattered electron (BSE) and secondary electron (SE) images (Tescan VEGA scanning electron microscope, Charles University, Czech Republic). Compositional mapping for Y, La, Th and U was performed on selected grains using an EPMA (Charles University, Czech Republic). Representative BSE images showing the position of dated monazite and/or internal zoning, and X-ray maps of Th and Y are shown in Figs. 9 and 10. Compositional mapping of monazite was done prior to analysis in samples PS118C and PV256B, but after the analysis in sample PV274B, therefore for this sample we present processed images of compositional maps.

Monazite and xenotime U/Th–Pb and REE data were measured at the Department of Earth Science, University of California, Santa Barbara, via laser ablation–split-stream inductively coupled plasma–mass spectrometry (LASS), which allows simultaneous isotopic and elemental analysis from the same mineral volume. The analytical procedure followed methods after Kylander-Clark et al. (2013) and Kylander-Clark (2017), and was applied as described in Štípská et al. (2020). Analyses of unknowns were bracketed by analyses of monazite primary reference materials (RM) 44,069 (424.9 ± 0.4 Ma Pb/U TIMS date; Aleinikoff et al., 2006). A secondary monazite reference material 'Stern' (512.1 ± 1.9 Ma; acquired from R. Stern, sample number 8153 sourced from the Bananeira I Pegmatite in Brazil, see also Palin et al., 2013; Horstwood et al., 2016) was also included as a monitor of accuracy and returned an age of 509.5 ± 1.8 Ma (95% C.I. internal precision).

The $^{238}U/^{206}Pb$ and $^{207}Pb/^{206}Pb$ isotopic ratios for each analysis were plotted on Tera–Wasserburg diagrams using *Isoplot* (Ludwig, 2003). For discordant U–Pb ratios we report a "^{207}Pb-corrected $^{238}U/^{206}Pb$ date" (Compston et al., 1992) by assuming a Stacey and Kramers (1975) common-Pb value. The discordant analyses can be explained by the presence of common Pb with a $^{207}Pb/^{206}Pb$ ratio consistent with the model of Stacey and Kramers (1975), and therefore, we use also the intercept dates calculated with the discordant analyses, which are comparable to dates calculated using the concordant analyses. It is supposed that the common Pb in the discordant analyses originates from inclusions and fractures in the monazite or from the Pb incorporated into the monazite during growth or recrystallization (Holder et al., 2015). The uncertainty for each isotopic ratio or spot date is reported at the 95%

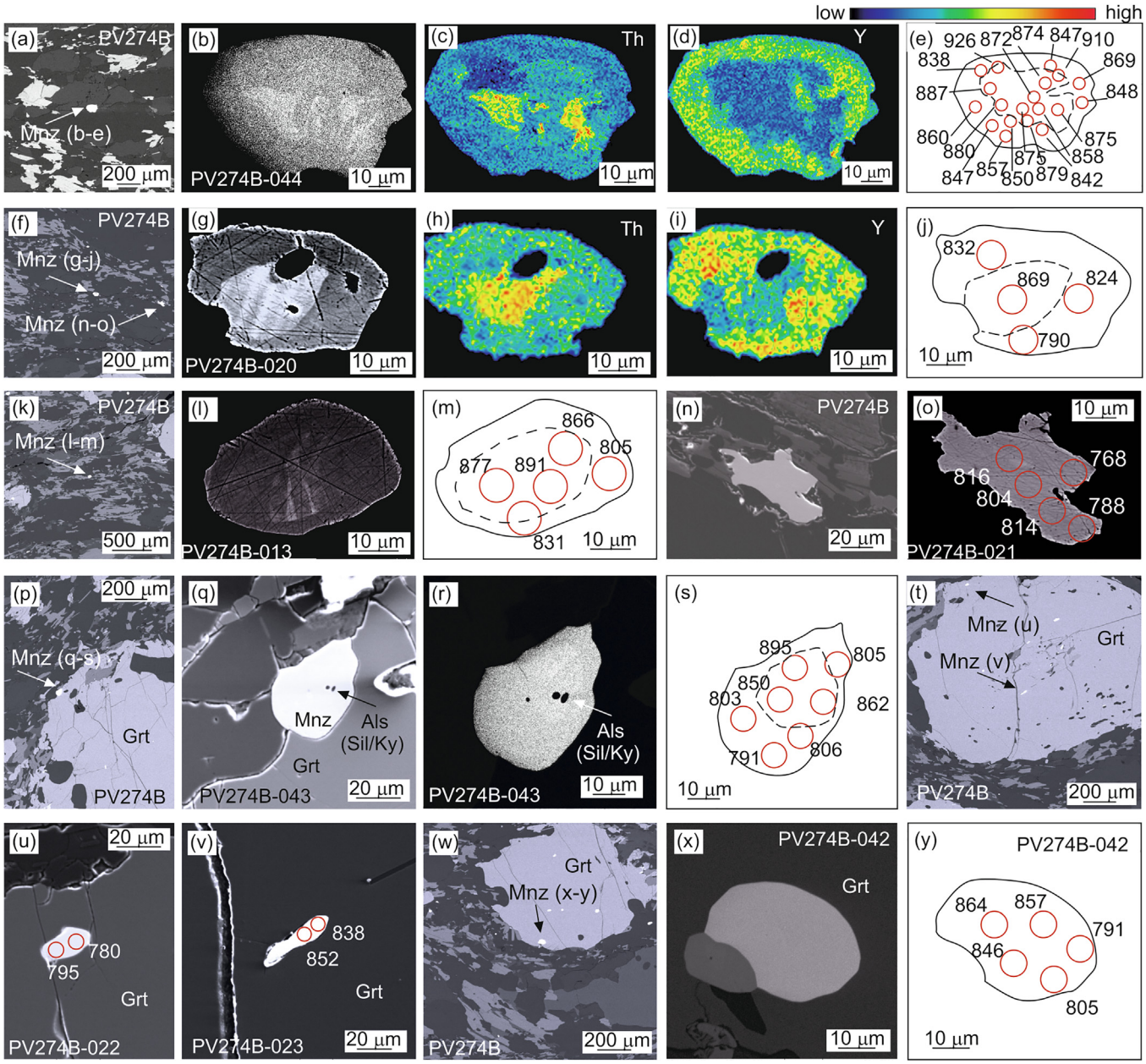

Fig. 9. Backscattered electron (BSE) images and compositional maps of representative monazite grains from Grt-Sil-Ky gneiss PV274B. Shown are monazite textural positions, close-up BSE images with analytical number of the monazite grain, Th- and Y-compositional maps and sketches with analytical points (10 µm) and resulting dates. (a–o) Matrix monazite; (p–y) Monazite included in garnet. For details see text.

confidence interval for the in-run uncertainty, assuming a Gaussian distribution of measurement errors. All of the analyses were obtained in an 11-day session, from which the samples PV274B and PV256B were analyzed in a single 1 day session; consequently, to assess population statistics and compare dates among samples we use only the in-run uncertainties. The isotopic ratios do not have sufficient spread in U–Pb ratios to define a $^{207}Pb/^{206}Pb$ intercept, therefore the Stacey–Kramers (e.g. Stacey and Kramers, 1975) for common lead was used to calculate intercept dates (0.896 ± 0.001 for 926–700 Ma group of dates). The data are provided as supplement (Supplementary Data A). The results of the U–Pb dating, chondrite-normalized REE patterns and the HREE slope expressed as a chondrite-normalized Yb_N/Gd_N ratio (normalizing values from Barcheck et al., 2012) are presented in Figs. 11 and 12.

6.2. Results for Grt-Sil-Ky gneiss PV274B

Monazite was found in garnet, in the matrix, and in the leucosome, and xenotime was found in the matrix; 80 spots were analyzed in 13 monazite grains and 4 spots in one xenotime grain (Fig. 9). Five monazite grains up to 50 µm in size were analyzed in garnet (Fig. 9p–y); from these, 10 spots were measured on grains in their cores (Fig. 9r, s), or on grains where the surrounding garnet does not exhibit cracks (Fig. 9v), and 14 spots on grains at their rims or on grains where the surrounding garnet exhibits cracks (Fig. 9r, s and u). Thirty-seven spots were analyzed on seven grains up to 80 µm in the matrix and 19 spots were analyzed on one 150 µm large grain in the leucosome (Fig. 9a–e). Four spots were analyzed in one xenotime grain (40 µm in size) in the matrix.

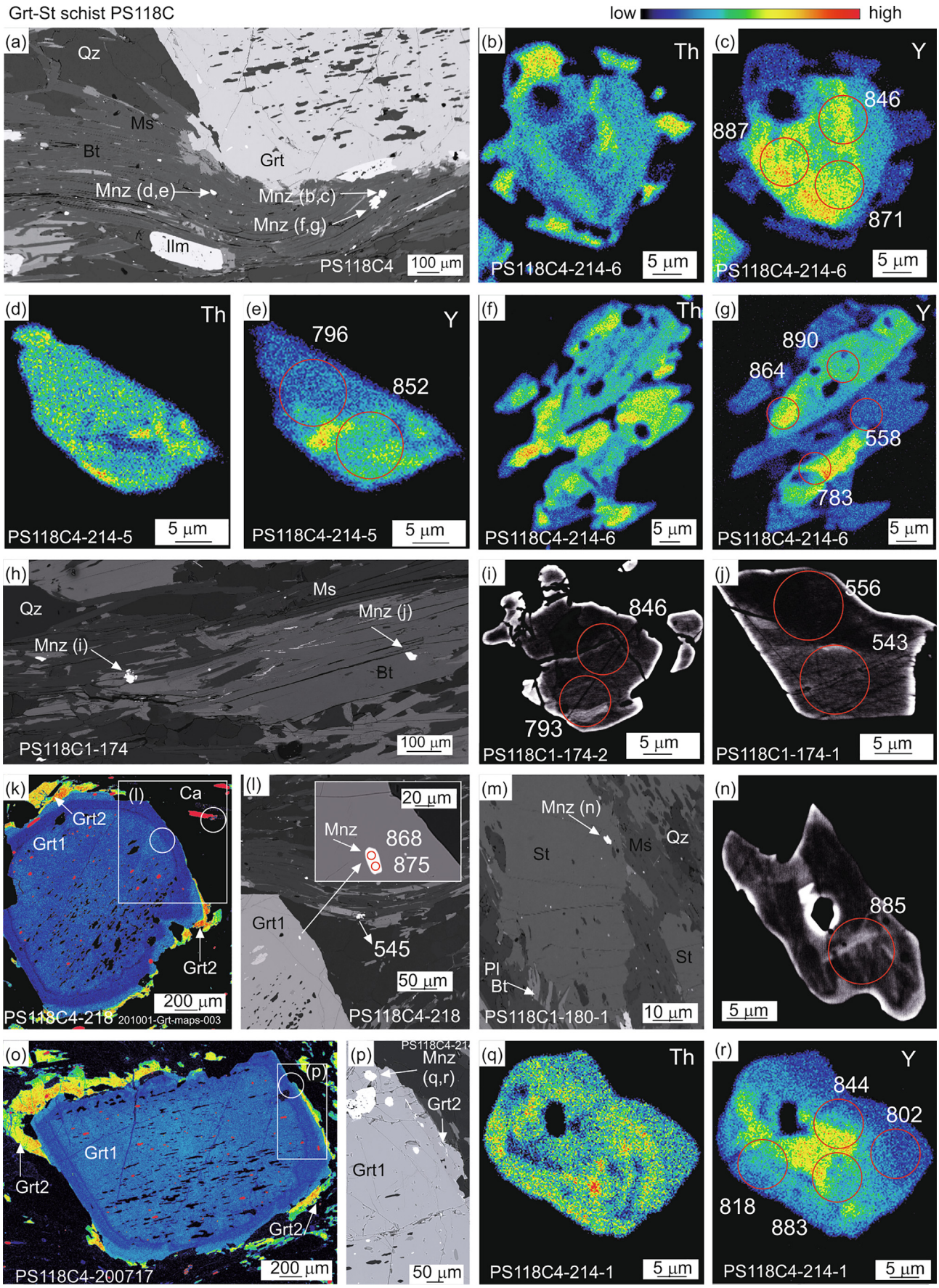
Grt-St schist PS118C
low
high
(a)
Qz
Ms
Bt
Grt
Mnz (d,e)
Mnz (b,c)
Mnz (f,g)
Ilm
PS118C4
100 µm
(b)
Th
PS118C4-214-6
5 µm
(c)
Y
846
887
871
PS118C4-214-6
5 µm
(d)
Th
PS118C4-214-5
5 µm
(e)
Y
796
852
PS118C4-214-5
5 µm
(f)
Th
PS118C4-214-6
5 µm
(g)
Y
890
864
558
783
PS118C4-214-6
5 µm
(h)
Qz
Ms
Mnz (i)
Mnz (j)
Bt
PS118C1-174
100 µm
(i)
846
793
PS118C1-174-2
5 µm
(j)
556
543
PS118C1-174-1
5 µm
(k)
(l)
Ca
Grt2
Grt1
Grt2
200 µm
PS118C4-218 201001-Grt-maps-003
(l)
20 µm
Mnz
868
875
Grt1
545
50 µm
PS118C4-218
(m)
Mnz (n)
St
Ms
Qz
St
Pl
Bt
PS118C1-180-1
10 µm
(n)
885
5 µm
(o)
(p)
Grt1
Grt2
Grt2
PS118C4-200717
200 µm
(p)
Mnz (q,r)
Grt2
Grt1
50 µm
(q)
Th
PS118C4-214-1
5 µm
(r)
Y
844
802
818
883
PS118C4-214-1
5 µm

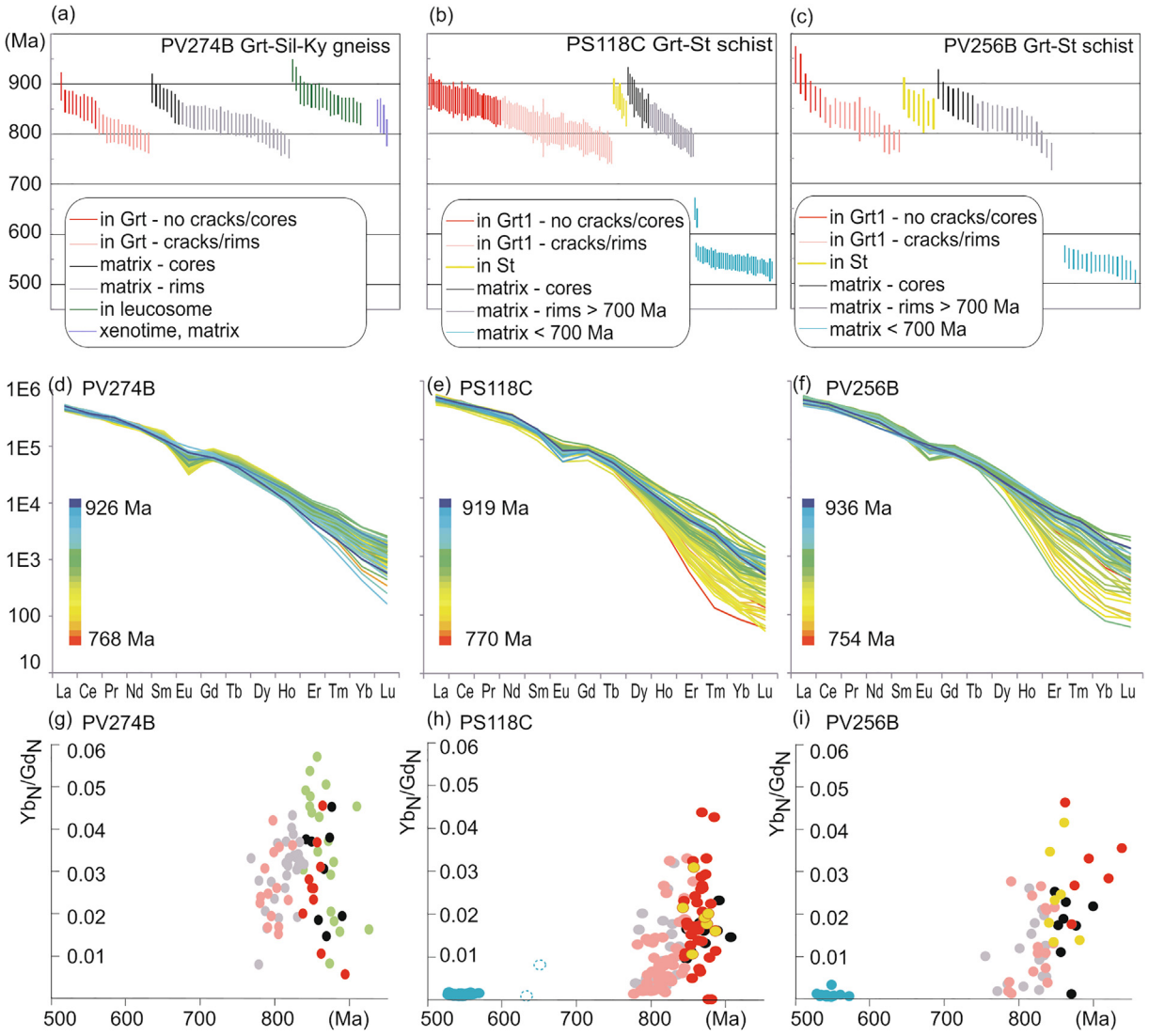

Fig. 11. LASS results of ^{207}Pb-corrected ^{238}U/^{206}Pb dates of monazite and xenotime. A Stacey and Kramers (1975) common-Pb value used is 0.896 ± 0.001 for 926–700 Ma group of dates, and 0.873 ± 0.001 for 568–515 Ma dates. Errors are 2 sigma. (a–c) Weighted mean plot of ^{207}Pb-corrected ^{238}U/^{206}Pb dates sorted by sample, textural position and decreasing age. (e–f) Chondrite-normalized REE patterns of monazite with colour keyed to age. (g–i) Variation of chondrite-normalized Yb_N/Gd_N vs. age sorted by textural position, colour legend is the same as for (a–c).

BSE images and compositional maps show variable zoning patterns (Fig. 9). Some grains have a light-grey BSE core or patches in the core, and a dark-grey BSE rim (e.g. Fig. 9b, g, l and r), others are homogeneous (Fig. 9o, x). Compositional maps show patchy zoning and irregular embayments, the grains with BSE-light-grey core have Th-richer and Y-poorer core compared to rim (Fig. 9c, d, h and i).

The monazite data yield a continuum of ^{207}Pb-corrected ^{238}U/^{206}Pb dates from 926 ± 22 Ma to 768 ± 19 Ma (2σ in-run uncertainties; Fig. 11a, d and 12a, e). In garnet, monazite cores or monazite in garnet without cracks is 895 ± 28 Ma to 838 ± 28 Ma, monazite rims or monazite in garnet that exhibits cracks is 824 ± 26 Ma to 780 ± 21 Ma. In the matrix, monazite is from 891 ± 29 Ma to 768 ± 19 Ma, monazite cores are from 891 ± 29 Ma to 842 ± 24 Ma and monazite rims are 840 ± 22 Ma to 768 ± 19 Ma. Monazite in the leucosome is 926 ± 22 Ma to 838 ± 22 Ma. Four spots on one xenotime grain in the matrix are 840 ± 25 Ma to 800 ± 25 Ma. In this sample, no monazite younger than 768 ± 19 Ma was found.

The relative probability distribution for all monazite spots does not show a single narrow peak, instead it shows a broad maxima from ca. 790 Ma to ca. 870 Ma (Fig. 12a, e). A peak at 865 Ma is observed for monazite from leucosome and a corresponding isochron is 869 ± 11 Ma (MSWD = 4.1, n = 19) (Fig. 12a, e). A peak at 870 Ma is observed for monazite cores in the matrix, with corresponding isochron 867 ± 9 Ma (MSWD = 1.3, n = 8), and a peak at 825 Ma with smaller peak at 790 Ma are observed for monazite rims in the matrix, an isochron calculated for this group is

Fig. 10. Backscattered electron (BSE) images and compositional maps of representative monazite grains from Grt-St schist PS118C. Shown are monazite textural positions, close-up BSE images, Th- and Y-compositional maps and analytical points (10 μm) with resulting dates. Analytical numbers of monazite grains are indicated. (a–j) Matrix monazite; (k, l) Monazite included in garnet1; (m, n) Monazite included in staurolite; (o–r) Monazite included in garnet1. For details see text.

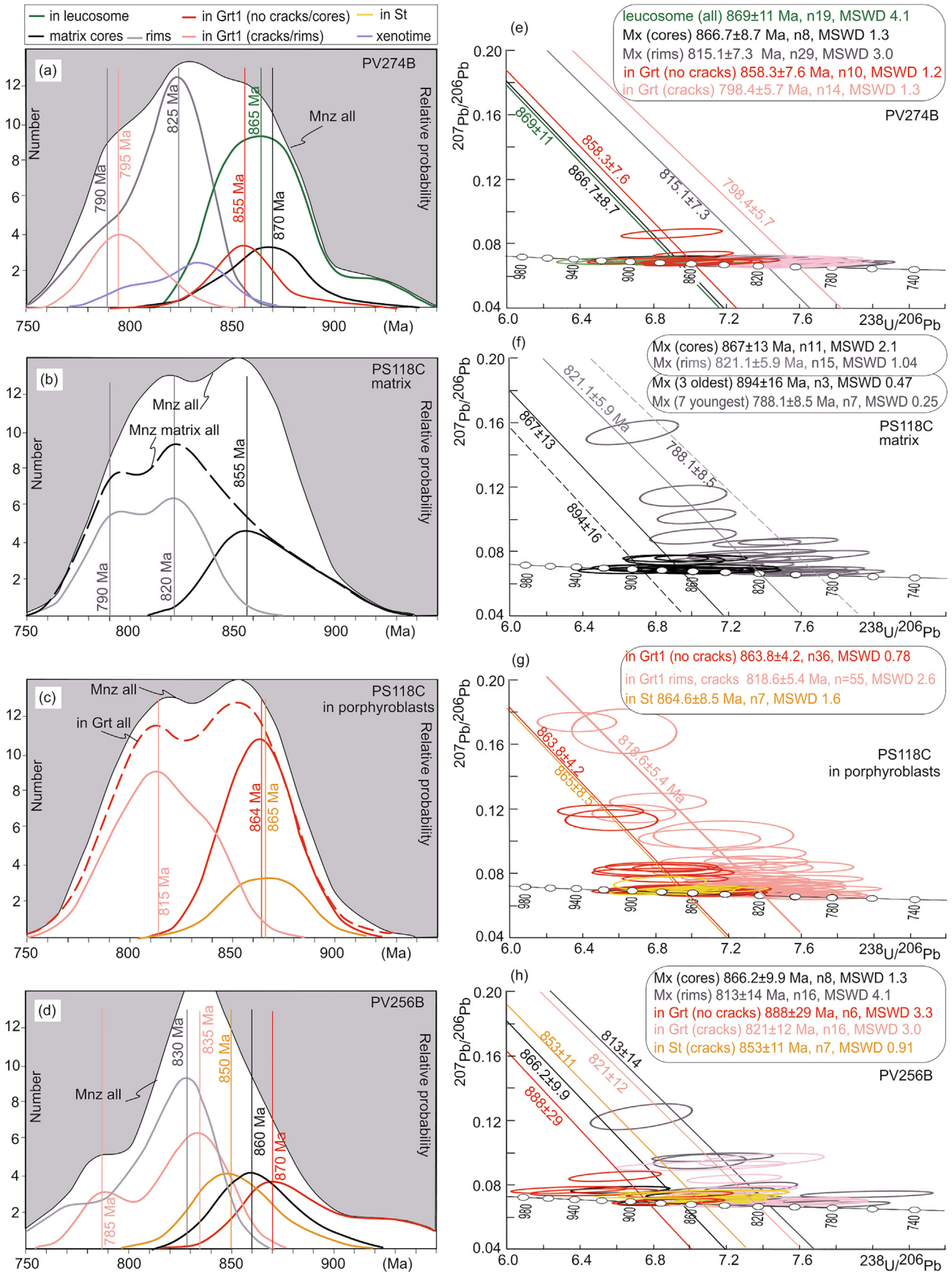

Fig. 12. LASS results of monazite and xenotime sorted by sample and textural position and shown (a–d) in probability density diagram of ^{207}Pb-corrected ^{238}U/^{206}Pb dates, dates indicate positions of peaks; (e–h) in Tera-Wasserburg concordia diagram. A Stacey and Kramers (1975) common-Pb value used is 0.896 ± 0.001, error ellipses are 2 sigma. For details see text.

815 ± 7 Ma (MSWD = 3, *n* = 29). For cores of monazite enclosed in garnet or for monazite in garnet without cracks, a peak at 855 Ma occurs, and a corresponding isochron is 858 ± 8 Ma (MSWD = 1.2, *n* = 10). For rims of monazite enclosed in garnet or for monazite in garnet that exhibits cracks the peak is at 795 Ma and corresponding isochron is 798 ± 6 Ma (MSWD = 1.3, *n* = 14). The relative probability distribution for matrix xenotime shows a peak at 835 Ma.

The monazite has relatively narrow spread in HREE and no clear variance of HREE concentration with age (Fig. 11d). Yb_N/Gd_N ratio is between 0.00 and 0.06 (Fig. 11g) without a systematic trend with textural position, and there is only a weak trend of narrower Yb_N/Gd_N range when plotted vs decreasing age.

6.3. Results for Grt-St schist PS118C

Monazite was found in garnet, staurolite and the matrix, and 171 spots were analyzed in 46 grains (Fig. 10). Twenty-seven monazite grains up to 40 μm in size were analyzed in garnet; from these, 36 spots were measured on grains in their cores, or on grains where the surrounding garnet does not exhibit cracks, 55 spots on grains in their rims or where the surrounding garnet exhibits cracks (Fig. 10k, l, o–r). Three grains (up to 40 μm) were analyzed in staurolite, 7 spots were measured (Fig. 10m, n). In the matrix, 15 monazite grains up to 40 μm were analyzed, 11 spots were measured on monazite cores and 62 spots were measured on monazite rims or on small grains (<20 μm) (Fig. 10a–j).

BSE images and compositional maps show a variety of zoning patterns, including patchy and irregular structures (Fig. 10b–g, n, q and r), and locally structure-less rims. Cores tend to have higher-Y compared to Y-poor rims, the boundary between the core and rim being diffuse (Fig. 10e), or sharp (Fig. 10c, g). Domains with lower Y tend to have higher Th content (Fig. 10b, c, f and g).

The data yield a continuum of ^{207}Pb-corrected $^{238}U/^{206}Pb$ dates from 905 ± 28 Ma to 536 ± 15 Ma (Fig. 11b). Monazite in garnet is 885 ± 29 Ma to 776 ± 21 Ma, monazite enclosed in staurolite is 885 ± 25 Ma to 847 ± 25 Ma, and monazite in the matrix shows two separate groups, first from 905 ± 28 Ma to 778 ± 22 Ma and second from 568 ± 14 Ma to 536 ± 15 Ma, and two outliers at 650–632 Ma. In this study, we will examine in detail only spots > 776 Ma.

The relative probability distributions plotted for all spots show two peaks at ca. 850 Ma and at ca. 820 Ma (line labelled "Mnz all" in Fig. 12b, c), and very similar peaks for all spots for the monazite enclosed in garnet (line "in Grt all" in Fig. 12c). For the matrix monazite cores, the relative probability distribution shows a peak at ca. 855 Ma and a related isochron is 867 ± 13 Ma (MSWD = 2.1, *n* = 11), an isochron plotted for the three oldest spots is 894 ± 16 Ma (MSWD = 0.47, *n* = 3) (Fig. 12b, f). For the matrix monazite rims, two smaller peaks occur at ca. 820 Ma and ca. 790 Ma, an isochron for older spots is 821 ± 6 Ma (MSWD = 1.04, *n* = 15), and an isochron of 788 ± 9 Ma (MSWD = 0.25, *n* = 7) is calculated for the 7 youngest spots (Fig. 12b, f). For monazite enclosed in garnet1 (Fig. 12c, g) without apparent cracks or for monazite cores, the dates range from 875 ± 27 Ma to 843 ± 24 Ma, a peak occurs at ca. 864 Ma and a related isochron is 864 ± 4 Ma (MSWD = 0.78, *n* = 36). For monazite enclosed in garnet1 with apparent cracks or spots at rims of grains the dates range from 855 ± 21 Ma to 776 ± 21 Ma, a peak occurs at ca. 815 Ma and a related isochron is 818 ± 5 Ma (MSWD = 2.6, *n* = 55). For monazite enclosed in staurolite, the relative probability distribution shows a peak at ca. 865 Ma and a related isochron is 865 ± 9 Ma (MSWD = 1.6, *n* = 7)(Fig. 12c, g).

The monazite shows a trend of lower HREE concentration with decreasing age for analyses older than 776 Ma (Fig. 11e). The Yb_N/Gd_N ratio for the group of dates 568–536 Ma is close to zero while the Yb_N/Gd_N spread for dates 905–776 Ma is between 0.00 and 0.05 (Fig. 11h). There is a trend of decreasing Yb_N/Gd_N ratio with age for monazite included in garnet and staurolite without apparent cracks to the matrix, compared to monazite enclosed in garnet1 with apparent cracks and rims of included monazite. A similar trend of decreasing Yb_N/Gd_N ratio when plotted against the age is observed for matrix monazite, with the majority of spots in monazite rims having lower Yb_N/Gd_N ratio compared to spots measured in monazite cores.

6.4. Results for garnet-staurolite schist PV256B

Monazite was found in garnet, staurolite and the matrix, and 71 spots were analyzed in 38 grains. Fifteen monazite grains up to 30 μm in size were analyzed in garnet; from these, 6 spots were measured on grains in their cores, or on grains where the surrounding garnet does not exhibit cracks, 16 spots on grains in their rims or where the surrounding garnet exhibits cracks. Four grains (up to 30 μm) were analyzed in staurolite and a total 7 spots were measured. In the matrix, 19 monazite grains up to 40 μm were analyzed, 8 spots were measured on monazite cores and 34 spots were measured on monazite rims or on small grains (<20 μm). BSE images show patchy and irregular structures and locally structure-less rims comparable to sample PS118C (not shown, for similar structures see Fig. 10).

The data yield a continuum of ^{207}Pb-corrected $^{238}U/^{206}Pb$ dates from 937 ± 37 Ma to 754 ± 27 Ma (Fig. 11c). Monazite in garnet is 937 ± 37 Ma to 785 ± 22 Ma, monazite enclosed in staurolite is 880 ± 31 Ma to 839 ± 30 Ma, and monazite in the matrix shows two separate groups, first from 899 ± 29 Ma to 754 ± 27 Ma and second from 560 ± 17 Ma to 515 ± 13 Ma. Further, we will examine in detail only spots > 754 Ma.

The relative probability distributions (Fig. 12d) plotted for all spots show one important peak at ca. 835 Ma and a small peak at ca. 785 Ma (line labelled "Mnz all" in Fig. 12d). For the matrix monazite cores, the relative probability distribution shows a peak at ca. 860 Ma and a related isochron is 866 ± 10 Ma (MSWD = 1.3, *n* = 8) (Fig. 12d, h). For the matrix monazite rims, two smaller peaks occur at ca. 830 Ma and ca. 770 Ma, a single isochron for all these spots is 813 ± 14 Ma (MSWD = 4.1, *n* = 16). For monazite enclosed in garnet1 without apparent cracks or monazite cores, the dates range from 937 ± 37 Ma to 861 ± 29 Ma, a peak occurs at ca. 870 Ma and a related isochron is 888 ± 29 Ma (MSWD = 3.3, *n* = 6). For monazite enclosed in garnet1 with apparent cracks, the dates range from 847 ± 25 Ma to 785 ± 22 Ma, one important peak occurs at c. 835 Ma and a smaller peak at ca. 785 Ma, a related isochron calculated for all these spots is 821 ± 12 Ma (MSWD = 3.0, *n* = 16). For monazite enclosed in staurolite, the relative probability distribution shows a peak at ca. 850 Ma and a related isochron is 853 ± 11 Ma (MSWD = 0.9, *n* = 7) (Fig. 12d, h).

The monazite shows a trend of lower HREE concentration with decreasing age for analyses older than 750 Ma (Fig. 11f). The Yb_N/Gd_N ratio for the group of ages 568–536 Ma is close to zero while the spread for ages between 937 Ma and 754 Ma is 0.00–0.05 (Fig. 11i). Yb_N/Gd_N ratio tends to decrease with age for monazite included in garnet and staurolite without apparent cracks to the matrix, compared to monazite enclosed in garnet1 with apparent cracks. Majority of spots in monazite rims have lower Yb_N/Gd_N ratio compared to spots measured in monazite cores.

7. Zircon geochronology

7.1. Methodology and sample preparation for U–Pb zircon dating

Zircons were obtained using conventional separation methods (crushing, Wilfley concentration table, magnetic and heavy liquid

separations) from ~5 kg per sample, then placed in epoxy mounts and polished. Internal textures were obtained by cathodoluminescence (CL) imaging using scanning electron microscope at the Czech Geological Survey in Prague.

The U–Pb dating of zircons was performed using Photon Machines Analyte Excite 193 nm excimer laser system equipped with a two-volume HelEx ablation cell that was connected to an Agilent 7900 quadrupole ICP-MS instrument at the Czech Geological Survey in Prague.

The analytical procedure was applied as described in Soejono et al. (2018). Data deconvolution using Iolite followed the method described by Paton et al. (2010), which involves subtraction of an 'on peak' gas blank followed by correction for laser-induced elemental fractionation (LIEF) by comparison with the behaviour of the 91500 reference zircon (Wiedenbeck et al., 1995), which yielded in this study concordia age of 1063.2 ± 3.0 Ma. No common Pb correction was applied. Zircon reference samples GJ-1 (ca. 609 Ma, Jackson et al., 2004) and Plešovice (ca. 337 Ma, Sláma et al., 2008) analysed during this study yielded concordia ages of 608.6 ± 2.6 Ma and 337.2 ± 2.0 Ma (2σ), respectively.

The zircon U–Pb ages are presented in concordia diagrams and in histograms with kernel density estimate generated with Isoplot v. 3.70 (Ludwig, 2003). Only analyses <5% discordant were taken into account. For the data interpretation, the $^{207}Pb/^{206}Pb$ age was used for zircons older than 1 Ga, while the $^{206}Pb/^{238}U$ age was used for zircons younger than 1 Ga. Maximum depositional ages (MDA) were calculated from the youngest zircon cluster following Dickinson and Gehrels (2009). These are presented as concordia ages calculated from the concordant youngest zircons that overlap in age at 1σ. U–Pb isotopic data, corresponding ages and Th/U ratios are provided as supplement (Supplementary Data B).

7.2. Results of U–Pb zircon dating for Grt-Sil-Ky gneiss PV274B

Zircon grains are mostly 60–100 μm long, generally shortly prismatic or stubby with subhedral crystal shapes. Most of the grains contain older corroded cores and distinct rims. The cores are ~20–50 μm in size and show variable internal textures from oscillatory to irregular convolute zoning (Fig. 13b). In contrast, the variously thick (5–60 μm) rims show generally weak oscillatory or sector zoning. Some grains also have thin bright outermost overgrowths. U–Pb zircon dating (89 concordant data from 191 analyses) yielded a wide spectrum of ages with a dominant younger peak at ca. 880 Ma, several minor peaks between ca. 1000 Ma and 2000 Ma and few ages around 2600 Ma (Fig. 13b). The Th/U ratios show systematic age and textural dependence. The older cores show uniformly higher Th/U ratios of ~0.3–1.2 compared to the youngest data obtained from the rims that have consistently very low Th/U ratios of < 0.06 (Fig. 13c). Such low Th/U ratios are generally considered as indicative of metamorphic zircon whereas the Th/U ratios higher than 0.1 are typical of magmatic zircon (e.g. Hoskin and Schaltegger, 2003; Rubatto, 2017). Weighted mean age 877 ± 7 Ma (2σ) calculated for the youngest rim-located age group (n = 36) is similar with lower intercepts of two best-fit discordia lines (lower inset in Fig. 13a). The maximum depositional age of the sedimentary protolith is determined by concordia age of 1372 ± 14 Ma (2σ) of the youngest overlapping data from the inherited detrital zircon cores (n = 4; upper inset in Fig. 13a). Few slightly younger ages around ca. 1100 Ma were obtained from the spots at or near the core-rim boundary and probably represent mixed ages or zircon affected by Pb-loss or partial metamorphic recrystallization.

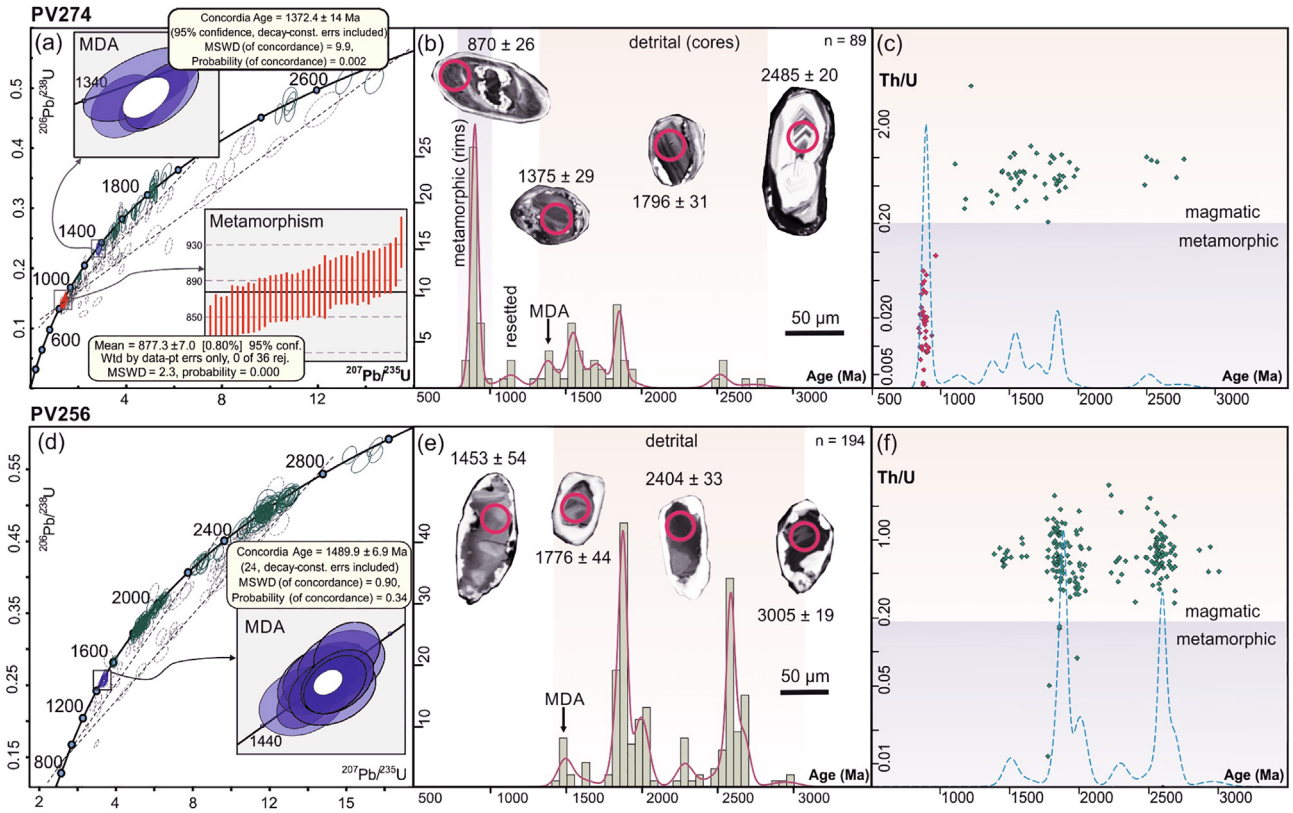

Fig. 13. (a, d) U–Pb concordia diagrams of the zircons from the studied metasedimentary samples PV274 and PV256 (data-point error symbols and ellipses are 2σ). Insets show calculated concordia or weighted mean $^{206}Pb/^{238}U$ ages ± 2σ. Dashed curves represent discordia regression lines among discordant analyses. (b, e) Frequency histograms with kernel density distributions of zircon age populations (n, number of analyses) with cathodoluminescence images of typical zircons. Laser dating spots with marked concordant $^{206}Pb/^{238}U$ ages ($^{207}Pb/^{206}Pb$ for ages > 1 Ga). (c, f) Th/U versus age plots. Dashed curves show kernel density distributions of zircon age populations.

7.3. Results of U–Pb zircon dating for garnet-staurolite schist PV256

Zircon grains are subhedral to anhedral, 70–150 μm long and shortly prismatic to isometric. CL internal patterns show cores with common oscillatory or sector zoning, or rarely unzoned cores, and variably thick and mostly bright rims (Fig. 13e). The zircon age population (194 concordant data from 263 analyses) shows a wide age group spreading from ca. 1400 Ma to 3000 Ma with dominant age peaks at ca. 1800 and 2600 Ma (Fig. 13d, e). In contrast to the previous sample, metamorphic rims were too small to be analysed. The concordia age of the minor youngest peak (n = 10) is 1490 ± 7 Ma and defines the maximum depositional age (inset in Fig. 13d). The discordant analyses define two discordia lines with a lower intercepts at ca. 880 Ma (Fig. 13d), similar to the weighted mean age of the youngest metamorphic zircons from sample PV274. The Th/U ratios generally range between ~0.3 and 2.0 (except few outliers) and there is no correlation between the age and Th/U ratios (Fig. 13f).

8. Discussion

8.1. The P-T paths and metamorphic gradients

The sequence of crystallization deduced from textures combined with garnet chemical zoning and mineral equilibria modelling allowed constraining the *P-T* paths from Grt-Sil-Ky gneiss and Grt-St schist (Fig. 14b). The inferred *P-T* paths therefore allow discussion of the evolution of the *P-T* gradients during metamorphism (Fig. 14b). The earliest parts of the *P-T* paths can be traced using garnet1 core compositions from ~660 °C and ~5.5 kbar for the Grt-Sil-Ky gneiss and from ~550 °C and ~4.5 kbar for the Grt-St schists. For the Grt-Sil-Ky gneiss, increase of *P-T* conditions to ~720 °C and ~6.0 kbar is inferred from garnet1 near rim composition, and is compatible with the succession of inclusions from Bt-Pl-Qz-Ilm to Sil-Bt-Pl-Qz-Ilm, indicating crossing the solidus, followed by crossing of the upper muscovite stability field. In the Grt-St schist, an increase to ~620 °C and ~6 kbar is inferred from garnet1 rim composition, compatible with the prograde appearance of garnet and staurolite, in the stability of ilmenite. This part of prograde *P-T* path (M1) in both types of samples occurred under similar and relatively high gradients of 27–32 °C/km.

The subsequent anticlockwise part of the *P-T* path (M2) to ~750 °C and ~9 kbar in the Grt-Sil-Ky gneiss is suggested by change in the mineral inclusion assemblage in garnet rims involving kyanite and rutile and also by garnet2 composition marked mainly by slight but systematic increase in grossular compared to garnet1. The profound reworking of the matrix in the kyanite stability field is supported by EBSD and XRD analysis of the mineral separate, which did not identify sillimanite. Similarly, an anticlockwise part of the *P-T* path to ~590 °C and 8.5 kbar is suggested in the Grt-St schist based on the texturally distinct garnet2 overgrowth on garnet1, marked mainly by a substantial increase in grossular. This nearly isothermal burial part of the *P-T* path (M2) occurred in both the Grt-Sil-Ky gneiss and Grt-St schist under markedly lower gradients of ~18–22 °C/km, compared to the M1 phase of metamorphism (Fig. 14b).

8.2. Monazite ages in the context of the P-T-t path

In-situ analysis of monazite included in porphyroblasts of garnet and staurolite allow discussion of the timing of porphyroblasts crystallization on the prograde path. The dates from monazite included in garnet and staurolite without apparent cracks to the matrix are interpreted as approximating the upper age limits for the growth of these porphyroblasts along the prograde path (e.g. following Štípská et al., 2015, 2020). The timing of further monazite (re)crystallization along the *P-T* path is based on monazite textures and chemical zoning. BSE images and compositional maps of monazite show variable patterns, some grains or domains are homogeneous, others are patchy or show concentric zoning, and in others the individual zones have embayed or sharp boundaries. In particular, the embayments of different monazite composition are considered as a result of recrystallization, typically caused by dissolution–precipitation in the presence of fluid or hydrous melt (e.g. Putnis, 2002; Kelly et al., 2012; Grand'Homme et al., 2016). The results of dating will be therefore considered as a possible result of recrystallization, not only monazite growth (e.g. following Štípská et al., 2015, 2020). This includes recrystallization of matrix monazite grains, but also recrystallization of monazite included in porphyroblasts, if the inclusions communicated with the matrix, for example along cracks.

The obtained monazite dates from Grt-Sil-Ky gneiss and Grt-St schists show a very large span from 937 Ma to 754 Ma, and in Grt-St schist also a group of dates between 568 Ma and 515 Ma. The group of 568–515 Ma dates, found only in Grt-St schists, is in agreement with the presence of Ediacaran–early Cambrian metamorphism documented on syn-tectonic magmatic rocks from the study area (e.g. Kozakov et al., 2006, 2008). The very large span of 937–754 Ma dates is in agreement with the observed monazite internal structural patterns indicating early crystallization followed by new crystallization or recrystallization along the *P-T* path during the Neoproterozoic. The inclusions of aluminosilicate in monazite with 895–850 Ma dates (Fig. 9q, r) support the metamorphic age of the monazite and exclude its detrital origin. Unfortunately, the inclusions are too small and did not provide EBSD patterns decisive for distinction between sillimanite and kyanite.

8.2.1. Monazite ages in the context of the P-T-t path, in Grt-Sil-Ky gneiss

In Grt-Sil-Ky gneiss, monazite in garnet without apparent cracks to the matrix is 895–838 Ma, and this time span is also compatible with monazite dates from the leucosome (926–838 Ma), and dates from the matrix monazite cores (891–842 Ma). The peaks and calculated isochrons for these groups of dates are in the range of 870–855 Ma, which can be considered as the approximate time of prograde metamorphism. Since garnet with monazite inclusions contains also sillimanite and monazite from the leucosome is of the same age; anatexis and metamorphic peak in the sillimanite stability also fall into this time span. Because of later (re)crystallization of monazite down to ca. 750 Ma, it is likely that some monazite dates, which we assigned to these groups based on internal monazite structures, were also affected by recrystallization. Therefore, the older age of ca. 870 Ma is considered as more realistic for the beginning of the prograde phase of metamorphism reaching a peak in the sillimanite stability at ~720 °C and ~6.5 kbar (Fig. 14b).

The overlapping age patterns of monazite in garnet and in leucosome are interpreted to represent a major period of monazite growth during prograde metamorphism, within the sillimanite stability field. This interpretation is based on empirical observations showing that monazite can grow semi-continuously along a prograde *P-T* path in Al-rich rocks. However, monazite tends to be small and irregular at the garnet isograd, more abundant, but small at the staurolite isograd, and abundant and large at the Al_2SiO_5 isograd (e.g. Kingsbury et al., 1993; Rubatto et al., 2001; Wing et al., 2003; Štípská et al., 2015, 2020; Yakymchuk et al., 2017). Thus in the Grt-Sil-Ky gneiss, growing garnet may have first included some rare prograde monazite, and later both sillimanite and monazite, representing the principal prograde monazite population. It was shown that when rocks enter suprasolidus conditions, monazite progressively dissolves in a partial melt with increasing

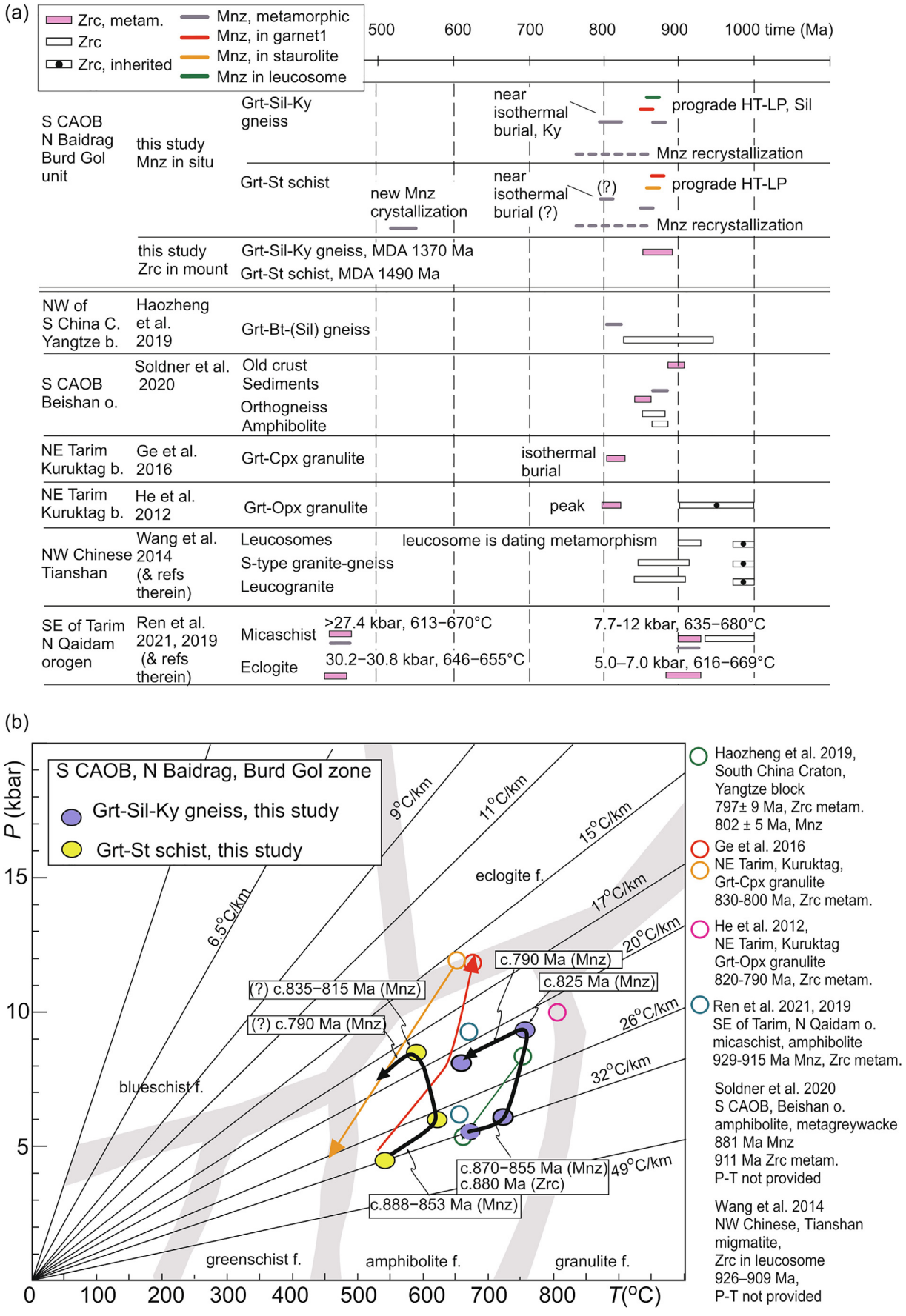

Fig. 14. Summary (a) and correlation (b) of inferred *P-T* conditions and zircon and monazite ages from this study with Stenian–Tonian *P-T* paths and their zircon and monazite ages reported from Asia.

temperature (e.g. Stepanov et al., 2012; Yakymchuk and Brown, 2014; Yakymchuk et al., 2017). Using the equations from Stepanov et al. (2012), Yakymchuk and Brown (2014) showed that < 5% of monazite is dissolved in melt at 720–760 °C in metapelite or metagreywacke with moderate to high LREE concentrations, leaving > 95% of prograde monazite preserved. This explains the abundant preservation of prograde monazite both in the garnet and leucosome of the Grt-Sil-Ky gneiss.

We did not find monazite included in garnet2 or in kyanite and therefore it is difficult to approximate time of burial into the Grt-Ky-Rt-bearing stability field. However, matrix monazite rims are 840–768 Ma, monazite in garnet that exhibits cracks is 824–780 Ma, and these data are compatible with 840–800 Ma dates from matrix xenotime. Hence, we interpret a peak at ca. 825 Ma for the matrix monazite rims as approximating the time of a major monazite recrystallization, and we associate it with a major metamorphic event that caused a pervasive recrystallization of the matrix to kyanite-bearing assemblage at ~770 °C and ~10 kbar (Fig. 14b). Smaller peaks occur for matrix monazite rims and monazite in garnet that exhibits cracks at ca. 790 Ma, indicating the end of monazite recrystallization, and which we consider as the approximate time of decompression and cooling (Fig. 14b). Because the youngest matrix monazite spot is 768 ± 19 Ma, it is clear that the garnet–kyanite–rutile-bearing assemblage is Tonian, and not Ediacaran or Cambrian. The analyses have narrower spread in HREE concentrations compared with samples of Grt-St schists. There is a trend into a narrower range of Yb_N/Gd_N ratio to 0.02–0.04 with decreasing age (Fig. 11g). This may be explained by the presence of melt and very similar mineral assemblage during both metamorphic phases in the sillimanite- and kyanite-stability fields. Similar are the findings of Stepanov et al. (2012) who described remarkably constant monazite/melt partitioning in experiments over large *P-T* span, and therefore interpreted variations in natural samples as originating from changes in the overall phase assemblage and/or the bulk composition. Nonetheless, the slightly lower maximum value of monazite Yb_N/Gd_N ratio of ca. 0.04 for the younger ages compared to ca. 0.06 for the older ages is compatible with an increase of the modal proportion of garnet during burial to the kyanite stability.

8.2.2. Monazite ages in the context of the P-T-t path, in Grt-St schist

The data from the two samples of Grt-St schists show very similar results and will be discussed together. Monazite enclosed in garnet1 without apparent cracks to the matrix is 937–843 Ma, monazite enclosed in staurolite is 885–839 Ma and matrix monazite cores are 905–846 Ma. The peaks and calculated isochrons for these groups of dates are in the range of 888–855 Ma, which can be considered as the approximate time of prograde metamorphism, however, based on the presence of old dates we consider the boundary of ca. 888 Ma as more probable for the early phase of prograde metamorphism. Another argument for considering the older dates as more reliable timing of prograde metamorphism is that monazite in these samples underwent (re)crystallization to ca. 754 Ma, and some of the spots that we assigned to these groups, based on monazite textural position and internal structures, may have also undergone partial recrystallization. For monazite enclosed in garnet1 with apparent cracks the dates range 855–776 Ma and for matrix monazite rims range 838–754 Ma. The peaks and calculated isochrons related to these groups range between 835 Ma and 815 Ma, and a smaller peak occurs at ca. 790 Ma. The group of 568–515 Ma dates is obtained on individual grains or on rims that show texturally sharp boundaries towards the Tonian monazite core. No monazite of Ediacaran–Cambrian age was found in garnet1 or staurolite, implying that the Tonian age for the prograde path to the staurolite stability field is robust.

We did not find any monazite grain in the garnet2, therefore, it is uncertain whether the garnet2 in the Grt-St schist grew during the Tonian or Cambrian. Nonetheless, if garnet2 is Tonian, the associated increase in pressure is comparable to the *P-T-t* path for the Grt-Sil-Ky gneiss. In this context, monazite minor peaks at 835–815 Ma may be related with monazite (re)crystallization during the second metamorphic phase of burial to 8.5 kbar and 590 °C. Minor peaks at ca. 790 Ma may be related with late monazite recrystallization on decompression and cooling. Another argument for linking these groups of dates with particular segments of the *P-T* path is the monazite chemical composition.

A trend of lower HREE concentration with decreasing age is typically interpreted as a result of garnet crystallization, which concentrates HREE (e.g. Wang et al., 2015). Monazite with 568–515 Ma dates have Yb_N/Gd_N ratio close to zero (Fig. 11h, i). This indicates that by the time of Ediacaran–Cambrian monazite growth, almost all the HREE were already tied in garnet (e.g. Wang et al., 2015), and that all the garnet was already grown by that time. Therefore, we consider the chemistry of the Ediacaran–Cambrian monazite to be in favor of garnet2 growth already in the Tonian. We speculate, that Ediacaran–Cambrian monazite growth may be related with superposed fluid input indicated by late chloritization.

In this interpretation, monazite dates with ca. 888–853 Ma peaks tend to have high HREE concentrations, and thus are dating the prograde part of the *P-T* path when the quantity of garnet has been low and was progressively increasing (Fig. 11e, f and 14b). The group of dates with 835–815 Ma peaks tends to have much lower HREE concentrations reflecting an already high amount of garnet that has been further increasing during burial to the kyanite stability field. The group of monazite with ca. 790 Ma peak has very low HREE concentration, reflecting the fact that almost all HREE have been tied in garnet and also in monazite, thus dating the retrograde *P-T* path. This is expressed also in a trend of decreasing Yb_N/Gd_N ratio with age for 905–776 Ma monazite. However, because of the indirect indications for the timing of the garnet2 growth, we present the Tonian ages for the second part of the *P-T* path for the Grt-St schist with a question mark (Fig. 14).

8.2.3. Evolution of geothermal gradients through time

Since there is no Cambrian monazite in the Grt-Sil-Ky gneiss, we consider the Tonian age for both phases of the *P-T* path as robust. Because monazite of Ediacaran–Cambrian age was not found in garnet1 or staurolite of the Grt-St schist, we consider the Tonian age for the prograde path to the staurolite stability field as also robust. We acknowledged the uncertainty about the age of the garnet2 growth in the Grt-St schist, but because of the indirect indications in favor of the Tonian garnet2 growth and therefore also Tonian age for the second part of the *P-T* path (Fig. 14), we will discuss the evolution of the geothermal gradients in the two type of samples together.

In samples with significantly different evolution of metamorphic assemblages to different peak *P-T* conditions, we found very similar range of dates for monazite included in prograde porphyroblasts, bracketing the burial of middle and lower crustal levels under high geothermal gradient of 27–32 °C/km to ca. 890–870 Ma. Similarly, for both the middle and lower crustal level very similar range of dates for (re)crystallized monazite brackets the second phase of metamorphism characterized by nearly isothermal burial at ~18–22 °C/km and following retrograde *P-T* path to 835–815 Ma. It is not clear exactly when the rocks reached the pressure peak because monazite recrystallization may have continued during decompression. It is also not clear whether the rocks stayed at depth under high geothermal gradient, and were exposed to long-lasting metamorphism accompanied with continuous (re)crystallization of monazite between these two phases of metamorphism,

or whether they underwent a phase of cooling and/or exhumation before subsequent burial.

The group of 568–515 Ma dates found in Grt-St schists supports the existence of a late Ediacaran–Cambrian phase of metamorphism, which may in this sample be related only to chloritization. However, we did not exclude completely the possibility, that garnet2 growth and therefore the burial at ~18–22 °C/km recorded in the Grt-St schist may be Ediacaran–Cambrian. In such a case, the Ediacaran–Cambrian phase of metamorphism would occur under remarkably similar metamorphic gradients as the evolution towards the end of the Tonian metamorphic history, recorded in the Grt-Sil-Ky gneiss.

8.3. Significance of U–Pb zircon data

The sedimentary age of the Burd Gol zone protolith has so far been only approximately constrained as Mesoproterozoic to Neoproterozoic on the basis of sporadic paleontological (Mitrofanov et al., 1981; Dergunov et al., 1997) and geochronological data (Demoux et al., 2009a). Similarly, both samples from this study show Mesoproterozoic calculated maximum depositional ages (1372 ± 14 Ma for PV274 and 1490 ± 7 Ma for PV256). Thus, our data confirm the previously proposed age of the metasedimentary Burd Gol unit.

With the exception of the youngest metamorphic ages of ca. 880 Ma, inferred from zircon microstructure and low Th/U ratios in the sample PV274, both samples have similar detrital zircon spectra only differing in the size of the individual age peaks. The detrital zircon populations can be divided into two major groups, a late Mesoproterozoic–early Paleoproterozoic part (1400–2100 Ma) and Neoarchean part (2400–2700 Ma). The samples also contain few scarce data at ca. 2300 and 3000 Ma. Similar Precambrian peaks of detrital zircon age patterns have been reported from several places in this part of CAOB and variously interpreted as crustal signature of either Siberia (Gladkochub et al., 2013; Glorie et al., 2014), Tarim (Rojas-Agramonte et al., 2011; Li et al., 2015) or Gondwana (Jiang et al., 2011; Yang et al., 2011; Zhou et al., 2018). The detrital zircon age populations of the two studied samples are not sufficient to identify the sedimentary provenance of the Burd Gol zone unambiguously.

Zircon rims gave a weighted mean age of 877 ± 7 Ma in sample of Grt-Sil-Ky gneiss as well as similar lower intercepts of two best-fit discordia lines, comparable to the oldest groups of monazite. These spot analysis have low Th/U values of ~0.01–0.06 (Fig. 13c), generally considered as indicative of metamorphic zircon (e.g. Hoskin and Schaltegger, 2003; Rubatto, 2017). The age of zircon rims and their chemical composition are therefore compatible with (re)crystallization of zircon during a high-temperature metamorphic event (lower inset in Fig. 13a). In the sample of Grt-St schist, the zircon rims were too small to be analysed, but the discordant analyses define two discordia lines with lower intercepts at ca. 880 Ma (Fig. 13d), similar to the weighted mean age of the metamorphic zircons from Grt-Sil-Ky gneiss, and to the oldest monazite groups, and therefore support the existence of a ca. 880 Ma metamorphic event in this rock. Zircon dating thus supports the timescale for metamorphism obtained from monazite dating in both samples.

8.4. Tonian metamorphism in the Baidrag margin compared to the southern CAOB

The inferred *P-T* paths are compared with *P-T* conditions and *P-T* paths from rocks with similar metamorphic ages, which are increasingly reported from various regions of the Tarim-North China collage (Fig. 14). They involve the Kuruktag block located NE of Tarim (He et al., 2012; Ge et al., 2016) and northern Qaidam orogen SE of Tarim (Ren et al., 2019, 2021) but also the Yangtze block in the NW part of the South China Craton (Haozheng et al., 2019).

In NE Tarim, He et al. (2012) calculated conditions of ~810 °C and 10 kbar for a garnet-orthopyroxene granulite and reported metamorphic zircon rims with 790–820 Ma ages. Ge et al. (2016) inferred an anticlockwise *P-T* path from garnet pyroxenite and garnet clinopyroxene gneiss, characterized by prograde burial associated with increase in temperature, followed by near-isothermal burial to 660–700 °C and 11–12 kbar, and retrograde exhumation. They interpreted the Tonian 830–800 Ma zircon ages as the time of retrograde metamorphism. Ren et al. (2019, 2021) documented an older Tonian metamorphic event in Silurian eclogites and surrounding schists from the SE part of the Tarim block. Here, the metamorphic conditions related to the Tonian event were based on mineral inclusions in garnet cores and in zircon, and revealed an amphibolite-facies event with *P-T* conditions of ~5.0–7.0 kbar and ~616–669 °C in an eclogite, and of ~7.7–12.0 kbar and ~634–680 °C in a garnet micaschist. Metamorphic zircon bracketed the age of amphibolite-facies phase in the eclogite to ca. 929–916 Ma. Zircon and monazite ages of ca. 920–915 Ma show that the garnet micaschist experienced the Tonian phase of metamorphism together with the enclosed eclogite.

Haozheng et al. (2019) reported 802 ± 5 Ma monazite and 797 ± 9 Ma metamorphic zircon ages for garnet–biotite–sillimanite rocks from the South China craton, with a peak at ~7–8 kbar and ~710 °C and retrograde conditions of ~5–6 kbar and ~650–675 °C. Metamorphic rocks with Tonian age were also reported from other areas, including for example migmatite from the NW Chinese Tianshan (Wang et al., 2014), and amphibolite and metagraywacke from the Beishan orogen in the southern CAOB (Soldner et al., 2020), however, for these rocks *P-T* conditions of metamorphism were not provided. Wang et al. (2014, and references therein) have shown based on zircon ages, that migmatization occurred at 926–909 Ma. Soldner et al. (2020) reported a zircon age of 911 ± 3 Ma obtained on metamorphic zircon rims in an amphibolite and a monazite age of ca. 881 ± 8 Ma related with garnet growth during a high-temperature metamorphic event of a metagraywacke.

The *P-T* paths from our samples show an early prograde evolution along relatively high geothermal gradients of 27–32 °C/km, that are comparable to geothermal gradients of 21–32 °C/km inferred from prograde paths or *P-T* peaks reported by Ge et al. (2016), Haozheng et al. (2019) and Ren et al. (2019). Our late metamorphic phase characterized by nearly isothermal burial and a peak pressure at geothermal gradient of ~ 18–22 °C/km correlates well with isothermal burial phase reported by Ge et al. (2016), who reported slightly higher peak pressure conditions and slightly lower geothermal gradient of ~ 15 °C/km (Fig. 14b).

8.5. Geodynamic implications

The petrological data reported in this work indicate a two stage evolution marked by early ca. 890–855 Ma hot and later ca. 835–815 Ma intermediate metamorphic gradient developed in a Mesoproterozoic sedimentary sequence. The early orogenic phase indicates HT conditions at low pressure typical for stretched crust of either a continental rift or back-arc–arc domain (Thompson et al., 2001). The pre-orogenic hot conditions and timing are comparable to those reported by Soldner et al. (2020) for the Beishan orogen, which have been interpreted to result from asthenospheric upwelling beneath the *peri*-Rodinian thinned continental margin. Importantly, the surface heat flow calculated for given *P-T* conditions yields values of 77–83 mW/m^2, which are compatible with a Cascadia type supra-subduction thinned continental margin (Curie and Hyndman, 2006; Hyndman, 2019). These conditions are

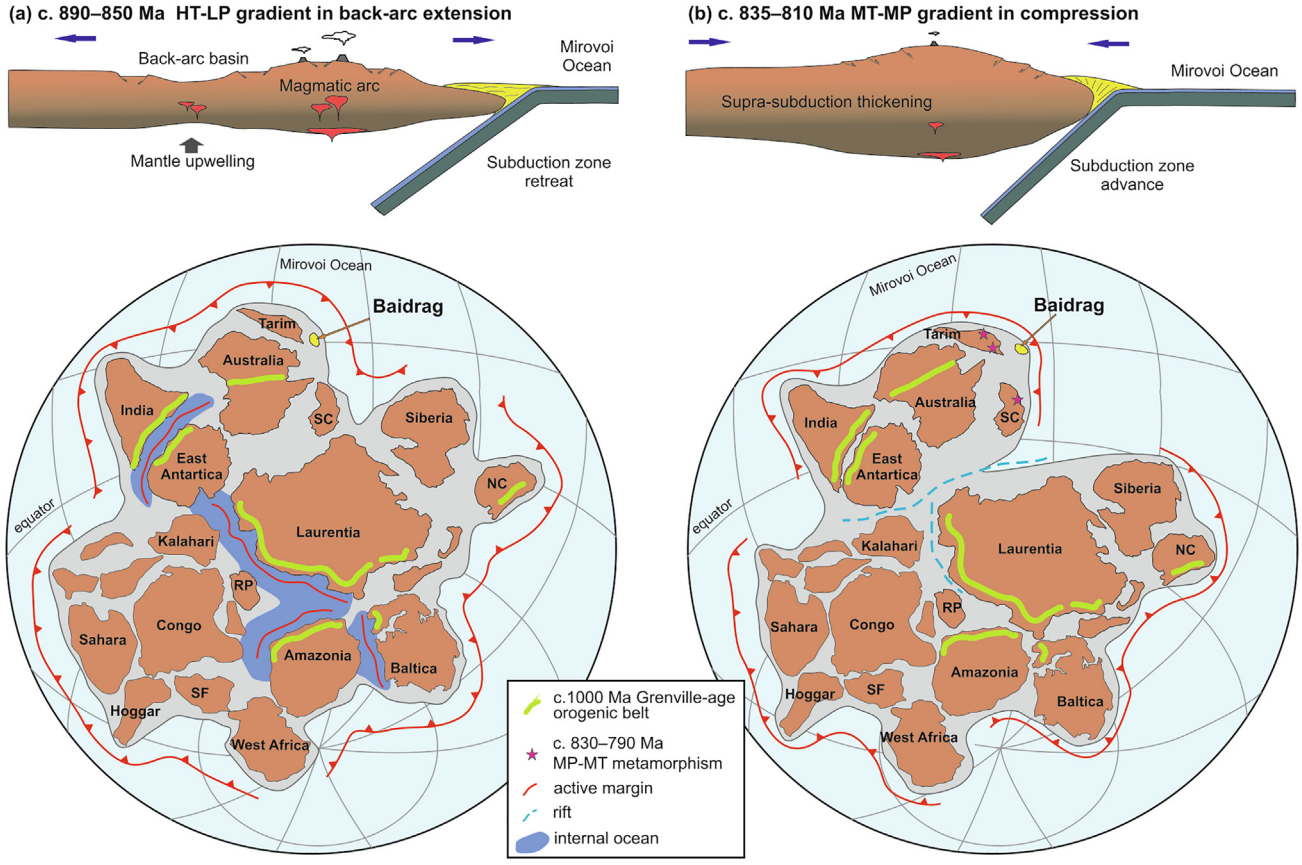

Fig. 15. Schematic tectonic models and paleogeographic reconstructions showing proposed Neoproterozoic evolution of the Baidrag block (modified after Metelkin et al., 2007; Li et al., 2008; Zhao et al., 2018). NC–North China Craton, SC–South China Craton, RP–Río de La Plata, SF–São Francisco.

compatible with active stretching of the upper plate and vigorous mantle convection above a retreating subduction zone (subduction roll-back stage of Collins, 2002) (Fig. 15a).

The second event is linked to important pressure increase up to 8.5–9 kbar associated with increasing temperature for both the studied samples at around 835–815 Ma. These *P-T* conditions and time scales can be compared to those reported in northern Tarim by Ge et al. (2016). These authors interpreted their *P-T-t* data to result from thickening of an earlier magmatic arc transformed to a fore-arc by subduction erosion and subsequent burial along bent isotherms near the subduction channel. Such an evolution can be achieved only if the progressively thickened hot crust receives additional heat at the bottom of the crust (Loosveld and Etheridge, 1990; Thompson et al., 2001), which is compatible with a model of arc or back-arc thickening accompanied with continuous magma underplating (Fig. 15b) (Collins, 2002; Soldner et al., 2022).

Altogether, the data presented in this work are compatible with the data previously acquired in the southern Tarim-North China collage, which show that during Neoproterozoic times occurred either supra-subduction back-arc stretching at 890–870 Ma (Soldner et al., 2020) or back-arc or arc thickening at 820–790 Ma (Ge et al., 2016). However, in the studied case both the evolutionary stages, involving formation of a hot supra-subduction crust and its thickening are reported at precisely the same time scales. Such an observation has a profound implication on the existing model of the circum-Rodinian active margin evolution and confirms the transition from subduction roll-back driven stretching mode to the subduction advancing mode related to thickening between 870 Ma and 815 Ma (Fig. 15).

Our data thus further complete the existing model of the agglomeration of the Rodinia supercontinent with a well-established peri-Rodinia accretion-thickening phase at 835–790 Ma (Fig. 15). In this context, the formation of Stenian–Tonian ophiolites (1050–900 Ma; Khain et al., 2002; Kuzmichev et al., 2005; Gordienko et al., 2009) represents a development of peripheral circum-Rodinian basins followed by a generalized continental margin stretching at 890–870 Ma (Li et al., 2008; Zhao et al., 2018; Soldner et al., 2020). This evolution along the periphery of Rodinia is coeval with the progressive closure of all internal Rodinian oceanic basins followed by climax of Tonian-aged continental collisional processes at the interior of the Rodinia supercontinent (Li et al., 2008; Cawood et al., 2016).

The 835–790 Ma event reflects the onset of circum-Rodinian shortening associated with onset of the rifting and progressive opening of the paleo-Pacific ocean following the end of the collisional intra-Rodinian (Tonian-aged) orogens. In analogy to other accretionary-collisional systems such as agglomeration of the Gondwana mega-continent and development of peripheral Terra Australis orogen (Cawood, 2005; Cawood and Buchan, 2007), the early hot gradient can be attributed to extension related to subduction roll-back at the super-continent margin when the internal Rodinia oceans were not yet entirely closed. On the other hand the later colder gradient can be related to the advancing or coupled mode of subduction. The mechanical coupling processes operating at the border of the super-continent reflect relocation of subductions following closure of all internal oceans from the supercontinent interior to its margin (Cawood and Buchan, 2007). This relocation is typically associated with opening of a new oceanic domain in the supercontinent interior (in this case paleo-Pacific)

and pushing of continental blocks against the peripheral ocean. As a consequence, the peripheral convergent boundary associated with hot thermal conditions experiences thickening and prograde metamorphism. In that sense the supra-subduction thickening event characterized in this work represents an important but overlooked aspect of the final construction of the Rodinia supercontinent.

9. Conclusions

(1) We describe for the first time ca. 890–790 Ma metamorphic cycle in the supracrustal rocks of the CAOB, from the NE margin of the Baidrag block in Mongolia.
(2) The anticlockwise *P-T* paths are inferred through thermodynamic modelling from sillimanite-bearing assemblage in garnet passing to kyanite-bearing assemblage in the matrix in a Grt-Sil-Ky gneiss, and from a Grt-St schist with two-stage garnet growth.
(3) The first phase of metamorphism is along a high geothermal gradient of 27–32 °C/km, and is related to an extensional setting at ca. 890–853 Ma inferred from monazite REE composition and monazite and zircon dating. The second phase of metamorphism is associated with burial at 18–22 °C/km and is related to compression at ca. 835–815 Ma based on monazite REE composition and dating. The exhumation is approximated from late monazite recrystallization to ca. 790 Ma.
(4) The age spectra of the detrital zircons define maximum depositional ages of 1372 ± 14 Ma for Grt-Sil-Ky gneiss and 1490 ± 7 Ma for the Grt-St schist. The detrital zircon populations show two major groups, of 1400–2100 Ma and 2400–2700 Ma and few data at ca. 3000 Ma.
(5) The contrasting geothermal gradients related to change of tectonic regime from extension to compression are interpreted as reflecting supra-subduction switching at Rodinia boundary in the sense of Collins (2002).
(6) In analogy to other peripheral accretionary systems (for instance Terra Australis orogen, around Gondwana) the early hot gradient can be attributed to extension related to subduction roll-back associated to a retreating-mode accretionary orogen, while the later colder gradient to advancing mode of subduction. The two processes, when operating at the border of super-continent reflect relocation of subduction from the supercontinent interior to its margin associated with change to advancing-mode and transient coupling across the plate boundary resulting in compression of the upper plate (Cawood and Buchan, 2007).

Declaration of Competing Interest

The authors declare that they have no known competing financial interests or personal relationships that could have appeared to influence the work reported in this paper.

Acknowledgements

This work was supported by the Czech Science Foundation, Czechia (grant number 19-27682X to K.S.). P. Hanžl is thanked for providing the geological maps, and M. Štrba and F. Veselovský for preparation of zircon separates and XRD analysis. Some of the zircon geochronological data was collected by N. Cathelin from the University of Strasbourg during internships at the Czech Geological Survey.

Appendix A. Supplementary data

Supplementary data to this article can be found online at https://doi.org/10.1016/j.gsf.2022.101520.

References

Aleinikoff, J.N., Schenck, W.S., Plank, M.O., Srogi, L.A., Fanning, C.M., Kamo, S.L., Bosbyshell, H., 2006. Deciphering igneous and metamorphic events in high-grade rocks of the Wilmington complex, Delaware: Morphology, cathodoluminescence and backscattered electron zoning, and SHRIMP U-Pb geochronology of zircon and monazite. Bull. Geol. Soc. Am. 118, 39–64. https://doi.org/10.1130/B25659.1.

Barcheck, C.G., Wiens, D.A., van Keken, P.E., Hacker, B.R., 2012. The relationship of intermediate- and deep-focus seismicity to the hydration and dehydration of subducting slabs. Earth Plan. Sci. Lett. 349–350, 153–160. https://doi.org/10.1016/j.epsl.2012.06.055.

Bibikova, E.V., Baikova, V.S., Gorohovskii, B.M., Gracheva, T.V., Kirnozova, T.I., Kozakov, I.K., Kotov, A.B., 1990. Early Proterozoic boundary in the Baidrag Block in central Mongolia. Izv. Akad. Nauk SSSR Ser. Geol. 7, 57–62 (in Russian).

Bold, U., Crowley, J.L., Smith, E.F., Sambuu, O., Macdonald, F.A., 2016. Neoproterozoic to early Paleozoic tectonic evolution of the Zavkhan terrane of Mongolia: Implications for continental growth in the Central Asian orogenic belt. Lithosphere 8, 729–750. https://doi.org/10.1130/L549.1.

Broussolle, A., Štípská, P., Lehmann, J., Schulmann, K., Hacker, B.R., Holder, R., Kylander-Clark, A.R.C., Hanžl, P., Racek, M., Hasalová, P., Lexa, O., Hrdličková, K., Buriánek, D., 2015. *P-T-t-D* record of crustal-scale horizontal flow and magma-assisted doming in the SW Mongolian Altai. J. Metamorph. Geol. 33, 359–383. https://doi.org/10.1111/jmg.12124.

Buchan, C., Cunningham, D., Windley, B.F., Tomurhuu, D., 2001. Stuctural and lithological characteristics of the Bayankhongor ophiolite zone, Central Mongolia. J. Geol. Soc. London 158, 445–460. https://doi.org/10.1144/jgs.158.3.445.

Buchan, C., Pfander, J., Kröner, A., Brewer, T.S., Tomurtogoo, O., Tomurhuu, D., Cunningham, D., Windley, B.F., 2002. Timing of accretion and collisional deformation in the Central Asian Orogenic Belt: implications of granite geochronology in the Bayankhongor Ophiolite Zone. Chem. Geol. 192, 23–45. https://doi.org/10.1016/S0009-2541(02)00138-9.

Buriánek, D., Schulmann, K., Hrdličková, K., Hanžl, P., Janoušek, V., Gerdes, A., Lexa, O., 2017. Geochemical and geochronological constraints on distinct Early-Neoproterozoic and Cambrian accretionary events along southern margin of the Baydrag Continent in western Mongolia. Gondwana Res. 47, 200–227. https://doi.org/10.1016/j.gr.2016.09.008.

Cawood, P.A., 2005. Terra Australis Orogen: Rodinia breakup and development of the Pacific and Iapetus margins of Gondwana during the Neoproterozoic and Paleozoic. Earth Sci. Rev. 69, 249–279. https://doi.org/10.1016/j.earscirev.2004.09.001.

Cawood, P.A., Buchan, C., 2007. Linking accretionary orogenesis with supercontinent assembly. Earth Sci. Rev. 82, 217–256. https://doi.org/10.1016/j.earscirev.2007.03.003.

Cawood, P.A., Kröner, A., Collins, W.J., Kusky, T.M., Mooney, W.D., Windley, B.F., 2009. Accretionary orogens through Earth history. Geol. Soc. Spec. Publ. 318, 1–36. https://doi.org/10.1144/SP318.1.

Cawood, P.A., Strachan, R., Cutts, K., Kinny, P.D., Hand, M., Pisarevsky, S., 2010. Neoproterozoic orogeny along the margin of Rodinia: Valhalla orogen, North Atlantic. Geology 38, 99–102. https://doi.org/10.1130/G30450.1.

Cawood, P.A., Strachan, R.A., Pisarevsky, S.A., Gladkochub, D.P., Murphy, J.B., 2016. Linking collisional and accretionary orogens during Rodinia assembly and breakup: Implications for models of supercontinent cycles. Earth Plan. Sci. Lett. 449, 118–126. https://doi.org/10.1016/j.epsl.2016.05.049.

Cocks, L.R.M., Torsvik, T.H., 2007. Siberia, the wandering northern terrane, and its changing geography through the Palaeozoic. Earth Sci. Rev. 82, 29–74. https://doi.org/10.1016/j.earscirev.2007.02.001.

Collins, W.J., 2002. Hot orogens, tectonic switching, and creation of continental crust. Geology 30, 535–538. https://doi.org/10.1130/0091-7613(2002)030<0535:HOTSAC>2.0.CO;2.

Compston, W., Williams, I.S., Kirschvink, J.L., Zhang, Z., Ma, G., 1992. Zircon U-Pb ages for the early Cambrian time-scale. 149, 171-184, doi:10.1144/gsjgs.149.2.0171.

Curie, C.A., Hyndman, R.D., 2006. The thermal structure of subduction zone back arcs. J. Geophys. Res. B Solid Earth 111. https://doi.org/10.1029/2005JB004024.

Cutts, K.A., Kinny, P.D., Strachan, R.A., Hand, M., Kelsey, D.E., Emery, M., Friend, C.R.L., Leslie, A.G., 2010. Three metamorphic events recorded in a single garnet: Integrated phase modelling, in situ LA-ICPMS and SIMS geochronology from the Moine Supergroup, NW Scotland. J. Metamorph. Geol. 28, 249–267. https://doi.org/10.1111/j.1525-1314.2009.00863.x.

Demoux, A., Kröner, A., Badarch, G., Jian, P., Tomurhuu, D., Wingate, M.T.D., 2009a. Zircon ages from the Baydrag Block and the Bayankhongor Ophiolite Zone: Time constraints on Late Neoproterozoic to Cambrian subduction- and accretion-related magmatism in Central Mongolia. J. Geol. 117, 377–397. https://doi.org/10.1086/598947.

Demoux, A., Kröner, A., Liu, D.Y., Badarch, G., 2009b. Precambrian crystalline basement in southern Mongolia as revealed by SHRIMP zircon dating. Int. J. Earth Sci. 98, 1365–1380. https://doi.org/10.1007/s00531-008-0321-4.

Dergunov, A.B., Ryazantsev, A.V., Luneva, O.I., Rikhter, A.V., 1997. Structure and geological history of the Bayan-Khongor Zone, central Mongolia. Geotectonics 31, 132–140.

Dickinson, W.R., Gehrels, G.E., 2009. Use of U-Pb ages of detrital zircons to infer maximum depositional ages of strata: A test against a Colorado Plateau Mesozoic database. Earth Plan. Sci. Lett. 288, 115–125. https://doi.org/10.1016/j.epsl.2009.09.013.

Dolzodmaa, B., Osanai, Y., Nakano, N., Adachi, T., 2020. Zircon U–Pb geochronology and geochemistry of granitic rocks in central Mongolia. Mongolian Geoscientist 50, 23–44.

Evans, D.A.D., 2009. The palaeomagnetically viable, long-lived and all-inclusive Rodinia supercontinent reconstruction. Geol. Soc. Spec. Publ. 327, 371–404. https://doi.org/10.1144/SP327.16.

Evans, D.A.D., 2013. Reconstructing pre-Pangean supercontinents. Bull. Geol. Soc. Am. 125, 1735–1751. https://doi.org/10.1130/B30950.1.

Ge, R.F., Zhu, W.B., Wilde, S.A., 2016. Mid-Neoproterozoic (ca. 830–800 Ma) metamorphic *P-T* paths link Tarim to the circum-Rodinia subduction-accretion system. Tectonics 35, 1465–1488. https://doi.org/10.1002/2016tc004177.

Gladkochub, D.P., Nicoll, G., Stanevich, A.M., Mazukabzov, A.M., Sklyarov, E.V., Pisarevsky, S.A., Donskaya, T.V., Tait, J., 2013. Age and sources of late precambrian sedimentary sequences of the Southern Baikal Region: Results of the U-Pb LA-ICP-MS dating of detrital zircons. Dokl. Earth Sci. 450, 494–498. https://doi.org/10.1134/S1028334X13050097.

Glorie, S., De Grave, J., Buslov, M.M., Zhimulev, F.I., Safonova, I.Y., 2014. Detrital zircon provenance of early Palaeozoic sediments at the southwestern margin of the Siberian Craton: Insights from U-Pb geochronology. J. Asian Earth Sci. 82, 115–123. https://doi.org/10.1016/j.jseaes.2013.12.007.

Gordienko, I.V., Bulgatov, A.N., Lastochkin, N.I., Sitnikova, V.S., 2009. Composition and U-Pb isotopic age determinations (SHRIMP II) of the ophiolitic assemblage from the Shaman paleospreading zone and the conditions of its formation (North Transbaikalia). Dokl. Earth Sci. 429, 1420–1425. https://doi.org/10.1134/S1028334X09090025.

Grand'Homme, A., Janots, E., Seydoux-Guillaume, A.-M., Guillaume, D., Bosse, V., Magnin, V., 2016. Partial resetting of the U-Th-Pb systems in experimentally altered monazite: Nanoscale evidence of incomplete replacement. Geology 44, 431–434. https://doi.org/10.1130/G37770.1.

Haozheng, W., Oscar, L., Huafeng, Z., Hong, Z., Xi, C., Mingguo, Z., 2019. Recognition and significance of c. 800 Ma upper amphibolite to granulite facies metamorphism in metasedimentary rocks from the NW margin of the Yangtze Block. J. Geol. Soc. London 177, 424–441. https://doi.org/10.1144/jgs2019-035.

He, Z.Y., Zhang, Z.M., Zong, K.Q., Wang, W., Santosh, M., 2012. Neoproterozoic granulites from the northeastern margin of the Tarim Craton: Petrology, zircon U-Pb ages and implications for the Rodinia assembly. Precambr. Res. 212, 21–33. https://doi.org/10.1016/j.precamres.2012.04.014.

Höck, V., 1974. Coexisting phengite, paragonite and margarite in metasediments of the Mittlere Hohe Tauern, Austria. Contrib. Mineral. Petrol. 43, 261–273.

Höck, V., Frank, W., Hejl, E., Furtmueller, G., 2000. Petrology and cooling history of the Mt. Ushgoeg Range (Central Mongolia). in: Badarch, G., Jahn, B.M., (Eds.), IGCP-420 Continental Growth in the Phanerozoic: Evidence from Central Asia. Second Workshop, Abstracts and Excursion Guidebook, Ulaanbaatar, Mongolia. Geosciences Rennes, Hors Série, vol. 2, pp. 35–37.

Holder, R.M., Hacker, B.R., Kylander-Clark, A.R.C., Cottle, J.M., 2015. Monazite trace-element and isotopic signatures of (ultra)high-pressure metamorphism: Examples from the Western Gneiss Region, Norway. Chem. Geol. 409, 99–111. https://doi.org/10.1016/j.chemgeo.2015.04.021.

Holland, T.J.B., Green, E.C.R., Powell, R., 2021. A thermodynamic model for feldspars in $KAlSi_3O_8$-$NaAlSi_3O_8$-$CaAl_2Si_2O_8$ for mineral equilibrium calculations. J. Metamorph. Geol. 40, 587–600. https://doi.org/10.1111/jmg.12639.

Holland, T.J.B., Powell, R., 2011. An improved and extended internally consistent thermodynamic dataset for phases of petrological interest, involving a new equation of state for solids. J. Metamorph. Geol. 29, 333–383. https://doi.org/10.1111/j.1525-1314.2010.00923.x.

Horstwood, M.S.A., Košler, J., Gehrels, G., Jackson, S.E., McLean, N.M., Paton, C., Pearson, N.J., Sircombe, K., Sylvester, P., Vermeesch, P., Bowring, J.F., Condon, D. J., Schoene, B., 2016. Community-derived standards for LA-ICP-MS U-(Th-)Pb geochronology - uncertainty propagation, age interpretation and data reporting. Geostandards Geoanal. Res. 40, 311–332. https://doi.org/10.1111/j.1751-908X.2016.00379.x.

Hoskin, P.W.O., Schaltegger, U., 2003. The composition of zircon and igneous and metamorphic petrogenesis. In: Hanchar, J.M., Hoskin, P.W.O. (Eds.), Zircon. Reviews in Mineralogy & Geochemistry. Mineralogical Society of America, Washington, pp. 27–62.

Huang, Z., Long, X., Wang, X.C., Zhang, Y., Du, L., Yuan, C., Xiao, W., 2017. Precambrian evolution of the Chinese Central Tianshan Block: Constraints on its tectonic affinity to the Tarim Craton and responses to supercontinental cycles. Precambr. Res. 295, 24–37. https://doi.org/10.1016/j.precamres.2017.04.014.

Hyndman, R.D., 2019. Mountain building orogeny in precollision hot backarcs: North American Cordillera, India-Tibet, and Grenville Province. J. Geophys. Res. Solid Earth 124, 2057–2079. https://doi.org/10.1029/2018JB016697.

Jackson, S.E., Pearson, N.J., Griffin, W.L., Belousova, E.A., 2004. The application of laser ablation-inductively coupled plasma-mass spectrometry to in situ U-Pb zircon geochronology. Chem. Geol. 211, 47–69. https://doi.org/10.1016/j.chemgeo.2004.06.017.

Jahn, B., Capdevila, R., Liu, D., Vernon, A., Badarch, G., 2004. Sources of Phanerozoic granitoids in the transect Bayanhongor-Ulaan Baatar, Mongolia: geochemical and Nd isotopic evidence, and implications for Phanerozoic crustal growth. J. Asian Earth Sci. 23, 629. https://doi.org/10.1016/S1367-9120(03)00125-1.

Jedlička, R., Faryad, S.W., Hauzenberger, C., 2015. Prograde metamorphic history of UHP granulites from the Moldanubian Zone (Bohemian Massif) revealed by major element and Y + REE zoning in garnets. J. Petrol. 56, 2069–2088. https://doi.org/10.1093/petrology/egv066.

Jian, P., Kröner, A., Windley, B.F., Shi, Y., Zhang, F., Miao, L., Tomurhuu, D., Zhang, W., Liu, D., 2010. Zircon ages of the Bayankhongor ophiolite mélange and associated rocks: Time constraints on Neoproterozoic to Cambrian accretionary and collisional orogenesis in Central Mongolia. Precambr. Res. 177, 162–180. https://doi.org/10.1016/j.precamres.2009.11.009.

Jiang, Y.D., Štípská, P., Sun, M., Schulmann, K., Zhang, J., Wu, Q.H., Long, X.P., Yuan, C., Racek, M., Zhao, G.C., Xiao, W.J., 2015. Juxtaposition of Barrovian and migmatite domains in the Chinese Altai: a result of crustal thickening followed by doming of partially molten lower crust. J. Metamorph. Geol. 33, 45–70. https://doi.org/10.1111/jmg.12110.

Jiang, Y.D., Schulmann, K., Sun, M., Weinberg, R.F., Štípská, P., Li, P.F., Zhang, J., Chopin, F., Wang, S., Xia, X.P., Xiao, W.J., 2019. Structural and geochronological constraints on Devonian suprasubduction tectonic switching and Permian collisional dynamics in the Chinese Altai, Central Asia. Tectonics 38, 253–280. https://doi.org/10.1029/2018TC005231.

Jiang, Y., Sun, M., Zhao, G., Yuan, C., Xiao, W., Xia, X., Long, X., Wu, F., 2011. Precambrian detrital zircons in the Early Paleozoic Chinese Altai: their provenance and implications for the crustal growth of central Asia. Precambr. Res. 189, 140–154. https://doi.org/10.1016/j.precamres.2011.05.008.

Kelly, N.M., Harley, S.L., Möller, A., 2012. Complexity in the behavior and recrystallization of monazite during high-T metamorphism and fluid infiltration. Chem. Geol. 322–323, 192–208. https://doi.org/10.1016/j.chemgeo.2012.07.001.

Kelty, T.K., Yin, A., Dash, B., Gehrels, G.E., Ribeiro, A.E., 2008. Detrital-zircon geochronology of Paleozoic sedimentary rocks in the Hangay-Hentey basin, northcentral Mongolia: implications for the tectonic evolution evolution of the Mongol-Okhotsk Ocean in central Asia. Tectonophysics 451, 290–311. https://doi.org/10.1016/j.tecto.2007.11.052.

Khain, E.V., Bibikova, E.V., Kröner, A., Zhuravlev, D.Z., Sklyarov, E.V., Fedotova, A.A., Kravchenko-Berezhnoy, I.R., 2002. The most ancient ophiolite of the Central Asian fold belt: U-Pb and Pb-Pb zircon ages for the Dunzhugur Complex, Eastern Sayan, Siberia, and geodynamic implications. Earth Plan. Sci. Lett. 199, 311–325. https://doi.org/10.1016/S0012-821X(02)00587-3.

Kingsbury, J.A., Miller, C.F., Wooden, J.L., Harrison, T.M., 1993. Monazite paragenesis and U-Pb systematics in rocks of the eastern Mojave Desert, California, U.S.A.: implications for thermochronometry. Chem. Geol. 110, 147–167. https://doi.org/10.1016/0009-2541(93)90251-D.

Kotov, A.B., Kozakov, I.K., Bibikova, E.V., Sal'nikova, E.B., Kirnozova, T.I., Kovach, V.P., 1995. Duration of regional metamorphic episodes in areas of polycyclic endogenic processes: a U-Pb geochronological study. Petrology 3, 567–575.

Kovach, V.P., Jian, P., Yarmolyuk, V.V., Kozakov, I.K., Kovalenko, V.I., Liu, D.Y., Terent'eva, L.B., 2005. Magmatism and geodynamics of early stages of the Paleoasian ocean formation: Geochronological and geochemical data on ophiolites of the Bayan-Khongor zone. Dokl. Earth Sci. 404, 1072–1077.

Kovalenko, V.I., Yarmolyuk, V.V., Tomurtogoo, O., Antipin, V.S., Kovach, V.P., Kotov, A.B., Kudryashova, E.B., Sal'nikova, E.B., Zagornaya, N.Y., 2005. Geodynamics and crust-forming processes in the early Caledonides of the Bayanhongor Zone, central Mongolia. Geotectonics 39, 298–316.

Kozakov, I.K., Sal'nikova, E.B., Yakovleva, S.Z., Plotkina, Y.V., Fedoseenko, A.M., 2006. Vendian metamorphism in the accretionary-collisional structure of central Asia. Dokl. Earth Sci. 407, 192–197. https://doi.org/10.1134/S1028334X06020073.

Kozakov, I.K., Sal'nikova, E.B., Wang, T., Didenko, A.N., Plotkina, Y.V., Podkovyrov, V. N., 2007. Early Precambrian crystalline complexes of the Central Asian microcontinent: Age, sources, tectonic position. Stratigr. Geol. Correl. 15, 121–140. https://doi.org/10.1134/S0869593807020013.

Kozakov, I.K., Sal'nikova, E.B., Kovach, V.P., Yarmolyuk, V.V., Anisimova, I.V., Kozlovsky, A.M., Plotnika, Y.V., Myskova, T.A., Fedoseenko, A.M., Yakovleva, S. Z., Sugorakova, A.M., 2008. Vendian stage in formation of the early Caledonian superterrane in central Asia. Stratigr. Geol. Correl. 16, 360–382. https://doi.org/10.1134/S0869593808040023.

Kozakov, I.K., Yarmolyuk, V.V., Kovach, V.P., Bibikova, E.V., Kirnozova, T.I., Kozlovskii, A.M., Plotkina, Y.V., Fugzan, M.M., Lebedev, V.I., Erdenezhargal, C., 2012. The Early Baikalian crystalline complex in the basement of the Dzabkhan microcontinent of the Early Caledonian orogenic area, Central Asia. Stratigr. Geol. Correl. 20, 231–239. https://doi.org/10.1134/S0869593812030057.

Kozakov, I.K., Kovach, V.P., Bibikova, E.V., Kirnozova, T.I., Lykhin, D.A., Plotkina, Y.V., Tolmacheva, E.V., Fugzan, M.M., Erdenezhargal, C., 2014. Late Riphean episode in the formation of crystalline rock complexes in the Dzabkhan microcontinent: Geological, geochronologic, and Nd isotopic-geochemical data. Petrology 22, 480–506. https://doi.org/10.1134/S086959111405004X.

Kozakov, I.K., 1993. The early Precambrian in the Central Asian Fold Belt. Nauka, St. Petersburg (in Russian).

Kröner, A., Demoux, A., Zack, T., Rojas-Agramonte, Y., Jian, P., Tomurhuu, D., Barth, M., 2011. Zircon ages for a felsic volcanic rock and arc-related early Palaeozoic sediments on the margin of the Baydrag microcontinent, central Asian orogenic belt, Mongolia. J. Asian Earth Sci. 42, 1008–1017. https://doi.org/10.1016/j.jseaes.2010.09.002.

Kröner, A., Kovach, V., Belousova, E., Hegner, E., Armstrong, R., Dolgopolova, A., Seltmann, R., Alexeiev, D., Hoffmann, J., Wong, J., 2014. Reassessment of continental growth during the accretionary history of the Central Asian

Orogenic Belt. Gondwana Res. 25, 103–125. https://doi.org/10.1016/j.gr.2012.12.023.
Kurimoto, C., Tungalag, F., Bayarmandal, L., Ichinnorov, N., 1998. K-Ar ages of white micas from pelitic schists of the Bayankhongor area, west Mongolia. Bull. Geol. Surv. Jpn. 49, 19–23.
Kuzmichev, A.B., Bibikova, E.V., Zhuravlev, D.Z., 2001. Neoproterozoic (~800 Ma) orogeny in the Tuva-Mongolia Massif (Siberia): Island arc-continent collision at the northeast Rodinia margin. Precambr. Res. 110, 109–126. https://doi.org/10.1016/S0301-9268(01)00183-8.
Kuzmichev, A., Kröner, A., Hegner, E., Dunyi, L., Yusheng, W., 2005. The Shishkhid ophiolite, northern Mongolia: A key to the reconstruction of a Neoproterozoic island-arc system in central Asia. Precambr. Res. 138, 125–150. https://doi.org/10.1016/j.precamres.2005.04.002.
Kylander-Clark, A.R.C., 2017. Petrochronology by laser-ablation inductively coupled plasma mass spectrometry. Rev. Minral. Geochem. 83, 183–198. https://doi.org/10.2138/rmg.2017.83.6.
Kylander-Clark, A.R.C., Hacker, B.R., Cottle, J.M., 2013. Laser-ablation split-stream ICP petrochronology. Chem. Geol. 345, 99–112. https://doi.org/10.1016/j.chemgeo.2013.02.019.
Li, Z.X., Bogdanova, S.V., Collins, A.S., Davidson, A., De Waele, B., Ernst, R.E., Fitzsimons, I.C.W., Fuck, R.A., Gladkochub, D.P., Jacobs, J., Karlstrom, K.E., Lu, S., Natapov, L.M., Pease, V., Pisarevsky, S.A., Thrane, K., Vernikovsky, V., 2008. Assembly, configuration, and break-up history of Rodinia: A synthesis. Precambr. Res. 160, 179–210. https://doi.org/10.1016/j.precamres.2007.04.021.
Li, Z., Qiu, N., Chang, J., Yang, X., 2015. Precambrian evolution of the Tarim Block and its tectonic affinity to other major continental blocks in China: New clues from U-Pb geochronology and Lu-Hf isotopes of detrital zircons. Precambr. Res. 270, 1–21. https://doi.org/10.1016/j.precamres.2015.09.011.
Lister, G., Forster, M., 2009. Tectonic mode switches and the nature of orogenesis. Lithos 113, 274–291. https://doi.org/10.1016/j.lithos.2008.10.024.
Loosveld, R., Etheridge, M., 1990. A model for low pressure facies metamorphism during crustal thickening. J. Metamorph. Geol. 8, 257–267. https://doi.org/10.1111/j.1525-1314.1990.tb00472.x.
Ludwig, K.R., 2003. Isoplot 3.00. A Geochronological Toolkit for Microsoft Excel. 4, 1-70.
Metelkin, D.V., Vernikovsky, V.A., Kazansky, A.Y., 2007. Neoproterozoic evolution of Rodinia: constraints from new paleomagnetic data on the western margin of the Siberian Craton. Russ. Geol. Geophys. 48, 32–45. https://doi.org/10.1016/j.rgg.2006.12.004.
Mitrofanov, F.P., Bibikova, E.V., Gracheva, T., Kozakov, I.K., Sumin, L.V., Shuleshko, I.K., 1985. Archean isotopic age of grey tonalitic gneisses in Celedonian structures of central Mongolia. Dokl. Akad. Nauk USSR 284, 670–675. in Russian.
Mitrofanov, F.P., Kozakov, I.K., Palay, I.P., 1981. Precambrian of western Mongolia and southern Tuva. Transactions of the joint Soviet-Mongolian scientific research geological expedition, vol. 32. Leningrad, Nauka, 156 p. (in Russian).
Murphy, J.B., Nance, R.D., 1991. Supercontinent model for the contrasting character of late Proterozoic orogenic belts. Geology 19, 469–472. https://doi.org/10.1130/0091-7613(1991)019<0469:SMFTCC>2.3.CO;2.
Nance, R.D., Murphy, J.B., Santosh, M., 2014. The supercontinent cycle: A retrospective essay. Gondwana Res. 25, 4–29. https://doi.org/10.1016/j.gr.2012.12.026.
Orolmaa, D., Erdenesaihan, G., Borisenko, A.S., Fedoseev, G.S., Babish, V.V., Zhmodik, S.M., 2008. Permian-Triassic granitoid magmatism and metallogeny of the Hangayn (central Mongolia). Russ. Geol. Geophys. 49, 534–544.
Osozawa, S., Tsolmon, G., Majigsuren, U., Sereenen, J., Niitsuma, S., Iwata, N., Pavlis, T., Jahn, B.M., 2008. Structural evolution of the Bayanhongor region, west-central Mongolia. J. Asian Earth Sci. 33, 337–352. https://doi.org/10.1016/j.jseaes.2008.01.003.
Palin, R.M., Searle, M.P., Waters, D.J., Parrish, R.R., Roberts, N.M.W., Horstwood, M.S.A., Yeh, M.W., Chung, S.L., Anh, T.T., 2013. A geochronological and petrological study of anatectic paragneiss and associated granite dykes from the Day Nui Con Voi metamorphic core complex, North Vietnam: constraints on the timing of metamorphism within the Red River shear zone. J. Metamorph. Geol. 31, 359–387. https://doi.org/10.1111/jmg.12025.
Parfenov, L.M., Khanchuk, A.I., Badarch, G., Miller, R.J., Naumova, V.V., Nokleberg, W.J., Ogasawara, M., Prokopiev, A.V., Yan, H., 2003. Preliminary Northeast Asia geodynamics map, sheet 2, scale 1:5,000,000. US Geological Survey Open-File Report 03–205.
Paton, C., Woodhead, J.D., Hellstrom, J.C., Hergt, J.M., Greig, A., Maas, R., 2010. Improved laser ablation U-Pb zircon geochronology through robust downhole fractionation correction. Geochem. Geophys. Geosyst. 11, 1–36. https://doi.org/10.1029/2009GC002618.
Putnis, A., 2002. Mineral replacement reactions: From macroscopic observations to microscopic mechanisms. Mineral. Mag. 66, 689–708. https://doi.org/10.1180/0026461026650056.
Ren, Y.F., Chen, D.L., Zhu, X.H., Ren, Z.L., Gong, X.K., Luo, F.H., 2019. Two orogenic cycles recorded by eclogites in the Yuka-Luofengpo terrane: Implications for the Mesoproterozoic to early Paleozoic tectonic evolution of the North Qaidam orogenic belt, NW China. Precambr. Res. 333. https://doi.org/10.1016/j.precamres.2019.105449.
Ren, Y.F., Chen, D.L., Wang, H.J., Zhu, X.H., Bai, B.W., 2021. Grenvillian and early Paleozoic polyphase metamorphism recorded by eclogite and host garnet mica schist in the North Qaidam orogenic belt. Geosci. Front. 12,. https://doi.org/10.1016/j.gsf.2021.101170 101170.
Rojas-Agramonte, Y., Kroner, A., Demoux, A., Xia, X., Wang, W., Donskaya, T., Liu, D., Sun, M., 2011. Detrital and xenocrystic zircon ages from Neoproterozoic to Palaeozoic arc terranes of Mongolia: Significance for the origin of crustal fragments in the Central Asian Orogenic Belt. Gondwana Res. 19, 751–763. https://doi.org/10.1016/j.gr.2010.10.004.
Rubatto, D., 2017. Zircon: The metamorphic mineral. Rev. Minral. Geochem. 83, 261–295. https://doi.org/10.2138/rmg.2017.83.09.
Rubatto, D., Williams, I.S., Buick, I.S., 2001. Zircon and monazite response to prograde metamorphism in the Reynolds Range, central Australia. Contrib. Mineral. Petrol. 140, 458–468. https://doi.org/10.1007/PL00007673.
Rudnev, S.N., Izokh, A.E., Borisenko, A.S., Shelepaev, R.A., Orihashi, Y., Lobanov, K.V., Vishnevsky, A.V., 2012. Early Paleozoic magmatism in the Bumbat-Hairhan area of the Lake Zone in western Mongolia (geological, petrochemical, and geochronological data). Russ. Geol. Geophys. 53, 425–441. https://doi.org/10.1016/j.rgg.2012.03.004.
Rytsk, E.Y., Amelin, Y.V., Rizvanova, N.G., Krimsky, R.S., Mitrofanov, G.L., Mitrofanova, N.N., Perelyaev, V.I., Shalaev, V.S., 2001. Age of rocks in the Baikal-Muya foldbelt. Stratigr. Geol. Correl. 9, 315–326.
Scotese, C.R., 2009. Late Proterozoic plate tectonics and palaeogeography: A tale of two supercontinents, Rodinia and Pannotia. Geo. Soc. London Special Pub. 326 (1), 67–83.
Shatsky, V.S., Malkovets, V.G., Belousova, E.A., Skuzovatov, S.Y., 2015. Evolution history of the Neoproterozoic eclogite-bearing complex of the Muya dome (Central Asian Orogenic Belt): Constraints from zircon U-Pb age, Hf and whole-rock Nd isotopes. Precambr. Res. 261, 1–11. https://doi.org/10.1016/j.precamres.2015.01.013.
Skuzovatov, S., 2021. Nature and (in-)coherent metamorphic evolution of subducted continental crust in the Neoproterozoic accretionary collage of SW Mongolia. Geosci. Front. 12, 101097. https://doi.org/10.1016/j.gsf.2020.10.004.
Skuzovatov, S., Wang, K.L., Dril, S., Lee, H.Y., Iizuka, Y., 2019. Geochemistry, zircon U-Pb and Lu-Hf systematics of high-grade metasedimentary sequences from the South Muya block (northeastern Central Asian Orogenic Belt): Reconnaissance of polymetamorphism and accretion of Neoproterozoic exotic blocks in southern Siberia. Precambr. Res. 321, 34–53. https://doi.org/10.1016/j.precamres.2018.11.022.
Sláma, J., Košler, J., Condon, D.J., Crowley, J.L., Gerdes, A., Hanchar, J.M., Horstwood, M.S.A., Morris, G.A., Nasdala, L., Norberg, N., Schaltegger, U., Schoene, B., Tubrett, M.N., Whitehouse, M.J., 2008. Plešovice zircon – A new natural reference material for U-Pb and Hf isotopic microanalysis. Chem. Geol. 249, 1–35. https://doi.org/10.1016/j.chemgeo.2007.11.005.
Soejono, I., Čáp, P., Míková, J., Janoušek, V., Buriánek, D., Schulmann, K., 2018. Early Palaeozoic sedimentary record and provenance of flysch sequences in the Hovd Zone (western Mongolia): Implications for the geodynamic evolution of the Altai accretionary wedge system. Gondwana Res. 64, 163–183. https://doi.org/10.1016/j.gr.2018.07.005.
Soejono, I., Peřestý, V., Schulmann, K., Čopjaková, R., Svojtka, M., Štípská, P., Buriánek, D., Janoušek, V., Lexa, O., 2021. Structural, metamorphic and geochronological constraints on Palaeozoic multi-stage geodynamic evolution of the Altai accretionary wedge system (Hovd Zone, western Mongolia). Lithos 396. https://doi.org/10.1016/j.lithos.2021.106204.
Soldner, J., Yuan, C., Schulmann, K., Jiang, Y., Štípská, P., Zhang, Y., Huang, Z., Wang, X., 2022. Early Paleozoic Cascadia-type active-margin evolution of the Dunhuang block (NW China): Geochemical and geochronological constraints. GSA Bulletin 134 (9–10), 2503–2530. https://doi.org/10.1130/B36220.1.
Soldner, J., Yuan, C., Schulmann, K., Štípská, P., Jiang, Y.D., Zhang, Y.Y., Wang, X.Y., 2020. Grenvillean evolution of the Beishan Orogen, NW China: Implications for development of an active Rodinian margin. Geol. Soc. Am. Bull. 132, 1657–1680. https://doi.org/10.1130/b35404.1.
Stacey, J.S., Kramers, J.D., 1975. Approximation of terrestrial lead isotope evolution by a two-stage model. Earth Plan. Sci. Lett. 26, 207–221. https://doi.org/10.1016/0012-821X(75)90088-6.
Stepanov, A.S., Hermann, J., Rubatto, D., Rapp, R.P., 2012. Experimental study of monazite/melt partitioning with implications for the REE, Th and U geochemistry of crustal rocks. Chem. Geol. 300–301, 200–220. https://doi.org/10.1016/j.chemgeo.2012.01.007.
Štípská, P., Schulmann, K., Powell, R., 2008. Contrasting metamorphic histories of lenses of high-pressure rocks and host migmatites with a flat orogenic fabric (Bohemian Massif, Czech Republic): A result of tectonic mixing within horizontal crustal flow? J. Metamorph. Geol. 26, 623–646. https://doi.org/10.1111/j.1525-1314.2008.00781.x.
Štípská, P., Hacker, B.R., Racek, M., Holder, R., Kylander-Clark, A.R.C., Schulmann, K., Hasalová, P., 2015. Monazite dating of prograde and retrograde *P-T-d* paths in the Barrovian terrane of the Thaya window, Bohemian Massif. J. Pet. 56, 1007–1035. https://doi.org/10.1093/petrology/egv026.
Štípská, P., Závada, P., Collett, S., Kylander-Clark, A.R.C., Hacker, B.R., Tabaud, A.S., Racek, M., 2020. Eocene migmatite formation and diachronous burial revealed by petrochronology in NW Himalaya, Zanskar. J. Metamorph. Geol. 38, 655–691. https://doi.org/10.1111/jmg.12534.
Takahashi, Y., Arakawa, Y., Oyungerel, S., Naito, K., 2000. Geochronological data of granitoids in the Bayankhongor area, central Mongolia. Bull. Geol. Surv. Jpn. 51, 167–174.
Teraoka, Y., Suzuki, M., Tungalag, F., Ichinnorov, N., Sakamaki, Y., 1996. Tectonic framework of the Bayankhongor area, west Mongolia. Bull. Geol. Surv. Jpn. 47, 447–455.
Thompson, A.B., Schulmann, K., Ježek, J., Tolar, V., 2001. Thermally softened continental extensional zones (arcs and rifts) as precursors to thickened orogenic belts. Tectonophysics 332, 115–141. https://doi.org/10.1016/S0040-1951(00)00252-3.

Tomurtogoo, O., Gerel, O., 1999. Geotraverse through a terrane collage in southern Khangay. in: Badarch, G., Jahn, B.M., Tomurhuu, D. (Eds.), IGCP-420 Continental Growth in the Phanerozoic: Evidence from Central Asia. Second workshop excursion guidebook, Ulaanbaatar, Mongolia. Geosciences Rennes. Hors série 2, 3–91.

Tomurtogoo, O., Nakajima, T., Takahashi, Y., Minjin, C., Ichinnorov, N., Oyungerel, S., (Eds.), 1998. Geology of the Bayankhogor area. Miscellanous Map Series, Scale 1:200 000 L-47-IX, L-47-X, L47-XVI, L-47-XVII, L-47-XXIII, L-47-XXIV.

Tomurtogoo, O., 2002. Tectonic map of Mongolia at scale 1: 1,000,000. Ulaanbaatar, Mineral Resources Authority of Mongolia, Mongolian Academy of Sciences (CD-ROM with English summary).

Vonesenskaya, T.A., Dergunov, A.B., Dashdavaa, Z., 1992. New data on lithology and stratigraphy of the Lower Palaeozoic deposits of Khangai (Mongolia). Izvestiya Russ. Acad. Sci., Series Geol. 3, 34–39 (in Russian).

Wang, B., Liu, H., Shu, L., Jahn, B.M., Chung, S.L., Zhai, Y., Liu, D., 2014. Early Neoproterozoic crustal evolution in northern Yili Block: Insights from migmatite, orthogneiss and leucogranite of the Wenquan metamorphic complex in the NW Chinese Tianshan. Precambr. Res. 242, 58–81. https://doi.org/10.1016/j.precamres.2013.12.006.

Wang, J.M., Rubatto, D., Zhang, J.J., 2015. Timing of partial melting and cooling across the Greater Himalayan Crystalline Complex (Nyalam, central Himalaya): In-sequence thrusting and its implications. J. Pet. 56, 1677–1702. https://doi.org/10.1093/petrology/egv050.

White, R.W., Powell, R., 2002. Melt loss and the preservation of granulite facies mineral assemblages. J. Metamorph. Geol. 20, 621–632.

White, R.W., Powell, R., Holland, T.J.B., Johnson, T.E., Green, E.C.R., 2014a. New mineral activity-composition relations for thermodynamic calculations in metapelitic systems. J. Metamorph. Geol. 32, 261–286. https://doi.org/10.1111/jmg.12071.

White, R.W., Powell, R., Johnson, T.E., 2014b. The effect of Mn on mineral stability in metapelites revisited: New *a-x* relations for manganese-bearing minerals. J. Metamorph. Geol. 32, 809–828. https://doi.org/10.1111/jmg.12095.

Wiedenbeck, M., Alle, P., Corfu, F., Griffin, W.L., Meier, M., Oberli, F., Vonquadt, A., Roddick, J.C., Speigel, W., 1995. 3 natural zircon standards for U-Th-Pb, Lu-Hf, trace-element and REE analyses. Geostand. Newsl. 19, 1–23. https://doi.org/10.1111/j.1751-908X.1995.tb00147.x.

Wilhem, C., Windley, B.F., Stampfli, G.M., 2012. The Altaids of Central Asia: A tectonic and evolutionary innovative review. Earth-Sci. Rev. 113, 303–341. https://doi.org/10.1016/j.earscirev.2012.04.001.

Windley, B.F., Alexeiev, D., Xiao, W.J., Kröner, A., Badarch, G., 2007. Tectonic models for accretion of the Central Asian Orogenic Belt. J. Geol. Soc. 164, 31–47. https://doi.org/10.1144/0016-76492006-022.

Wing, B.A., Ferry, J.M., Harrison, T.M., 2003. Prograde destruction and formation of monazite and allanite during contact and regional metamorphism of pelites: petrology and geochronology. Contrib. Mineral. Petrol. 145, 228–250. https://doi.org/10.1007/s00410-003-0446-1.

Xiao, W.J., Windley, B.F., Sun, S., Li, J.L., Huang, B.C., Han, C.M., Yuan, C., Sun, M., Chen, H.L., 2015. A tale of amalgamation of three Permo-Triassic collage systems in Central Asia: Oroclines, sutures, and terminal sccretion. in: Jeanloz, R., Freeman, K.H. (Eds.), Annual Review of Earth and Planetary Sciences, 43, 477-507.

Xiao, W.J., Windley, B.F., Han, C.M., Liu, W., Wan, B., Zhang, J., Ao, S.J., Zhang, Z.Y., Song, D.F., 2018. Late Paleozoic to early Triassic multiple roll-back and oroclinal bending of the Mongolia collage in Central Asia. Earth-Sci. Rev. 186, 94–128. https://doi.org/10.1016/j.earscirev.2017.09.020.

Yakymchuk, C., Brown, M., 2014. Behaviour of zircon and monazite during crustal melting. J. Geol. Soc. London 171, 465–479. https://doi.org/10.1144/jgs2013-115.

Yakymchuk, C., Clark, C., White, R.W., 2017. Phase Relations, Reaction Sequences and Petrochronology. in: Kohn, M. J., Engi, M., Lanari, P. (Eds.), Petrochronology: Methods and Applications, 83, 13-53. Mineralogical Soc. Amer. & Geochemical Soc., Chantilly. doi:10.1515/9783110561890.

Yang, T.N., Li, J.Y., Zhang, J., Hou, K.J., 2011. The Altai-Mongolia terrane in the Central Asian Orogenic Belt (CAOB): A peri-Gondwana one? Evidence from zircon U-Pb, Hf isotopes and REE abundance. Precambr. Res. 187, 79–98. https://doi.org/10.1016/j.precamres.2011.02.005.

Yao, J., Cawood, P.A., Shu, L., Zhao, G., 2019. Jiangnan Orogen, South China: A ~970–820 Ma Rodinia margin accretionary belt. Earth Sci. Rev. 196. https://doi.org/10.1016/j.earscirev.2019.05.016.

Yarmolyuk, V.V., Kovalenko, V.I., Sal'nikova, E.B., Kovach, V.P., Kozlovsky, A.M., Kotov, A.B., Lebedev, V.I., 2008. Geochronology of igneous rocks and formation of the Late Paleozoic south Mongolian active margin of the Siberian continent. Stratigr. Geol. Correl. 16, 162. https://doi.org/10.1134/S0869593808020056.

Yarmolyuk, V.V., Kovach, V.P., Kovalenko, V.I., Salnikova, E.B., Kozlovskii, A.M., Kotov, A.B., Yakovleva, S.Z., Fedoseenko, A.M., 2011. Composition, sources, and mechanism of continental crust growth in the Lake zone of the Central Asian Caledonides: I. Geological and geochronological data. Petrology 19, 55–78. https://doi.org/10.1134/S0869591111010085.

Zhao, G., Wang, Y., Huang, B., Dong, Y., Li, S., Zhang, G., Yu, S., 2018. Geological reconstructions of the East Asian blocks: From the breakup of Rodinia to the assembly of Pangea. Earth Sci. Rev. 186, 262–286. https://doi.org/10.1016/j.earscirev.2018.10.003.

Zhou, J.B., Wilde, S.A., Zhao, G.C., Han, J., 2018. Nature and assembly of microcontinental blocks within the Paleo-Asian Ocean. Earth Sci. Rev. 186, 76–93. https://doi.org/10.1016/j.earscirev.2017.01.012.

Zonenshain, L.P., 1990. Geology of the USSR: a plate tectonic synthesis. Am. Geophys. Union. Geodyn. Monogr. 21, 1–242.